Electronic Structures of Active Sites on Metal Oxide Surfaces: Definition of the Cu/ZnO Methanol Synthesis Catalyst by Photoelectron Spectroscopy

Edward I. Solomon,* Paul M. Jones, and Jennifer A. May

Department of Chemistry, Stanford University, Stanford, California 94305

Received March 29, 1993 (Revised Manuscript Received August 12, 1993)

Contents

I. Introduction

Metal ion active sites play key roles in biological, homogeneous, and heterogeneous catalysis. Often these sites exhibit unique spectral features compared to small molecule inorganic complexes of the same metal ion. These derive from the fact that unusual geometric structures can be imposed on a metal ion through its interaction with the support and thus lead to novel electronic structures. These electronic structures can make significant contributions to the reactivity of active sites in catalysis. While this concept is general over the different areas of catalysis mentioned above, the spectroscopic methodology required to study active sites is dependent on the type of material involved in the support. In metalloenzymes one emphasizes methods such as electron paramagnetic resonance and magnetic circular dichroism spectroscopies which can probe a very dilute paramagnetic metal ion in a diamagnetic biopolymer host.[1] In the field of heterogeneous catalysis one is interested in studying the small concentration (10^{15} atoms/cm^2) of metal ion sites on the surface of a material and thus the emphasis is on surface-sensitive spectroscopic methods in particular photoelectron spectroscopy.[2-5] While photons can penetrate thousands of angstroms into a solid, the average escape depth of electrons from a material is highly dependent on their kinetic energy as shown by the curve in Figure 1; for energies in the range of 50 to 110 eV this will involve the top few angstroms of a material providing high surface sensitivity.[6] The focus of this review is on the use of photoelectron spectroscopy (PES) to study the interaction of small molecules (particularly carbon monoxide) with metal ion sites on metal oxide surfaces. There have been numerous photoemission studies of chemisorption on metal surfaces. However, it is important to note that while metal oxides are involved in many heterogeneous catalytic processes (Table I), only a limited number of electron spectroscopic studies of chemically relevant molecules on metal oxide surfaces have appeared (Table II).

Understanding the interaction of CO with ZnO surfaces is a particularly interesting and important problem from a variety of perspectives.[7] First it is a *unique inorganic complex*. Studies on metal surfaces involve CO binding to zerovalent metal sites to form organometallic surface species, a classic example being the CO/$[Ni]_{surface}$ complex.[8-10] Alternatively, for the CO/ZnO system, the metal ion is in the divalent oxidation state and surrounded by oxide ligands.[7] Thus one has an organometallic ligand binding to a classic coordination compound (or Werner) surface. Associated with this unusual inorganic complex are *unique spectral features*, including the CO stretching frequency obtained by IR studies of powders.[11,12] Binding CO to metal surfaces results in a decrease in the CO stretching frequency.[9] This behavior is generally observed in organometallic chemistry and associated with the participation of metal d electrons in backbonding into the $2\pi^*$ orbital of the CO molecule (vide infra). For the

0009-2665/93/0793-2623$12.00/0 © 1993 American Chemical Society

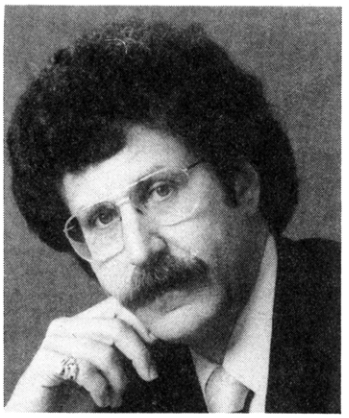

Edward I. Solomon is presently the Monroe E. Spaght Professor of Chemistry at Stanford University where he has been since 1982 and was previously a Professor at the Massachusetts Institute of Technology. Professor Solomon received his Ph.D. for research directed by Professor Donald S. McClure at Princeton University and then was a postdoctoral fellow working first with Professor C. J. Ballhausen at the H. C. Ørsted Institute at the University of Copenhagen and then with Professor Harry Gray at the California Institute of Technology. He is an associate editor of *Inorganic Chemistry* and a member of the editorial board of *Chemical Reviews*, *Inorganic Biochemistry*, and *Chemtracts*; he has been the first Glen Seaborg, Taiwan National Science Council, Xerox, O. K. Rice, Reilly, Frontiers and World Bank lecturer and an Invited Professor at at the University of Paris, Xiamen University (China), La Plata University (Argentina), and Tokyo Institute of Technology. He received the 1990 Deans Award for Distinguished Teaching at Stanford. His research interests included physical–inorganic chemistry, bioinorganic chemistry, and surface science with emphasis on the detailed spectroscopic study of transition metal ion electronic structure.

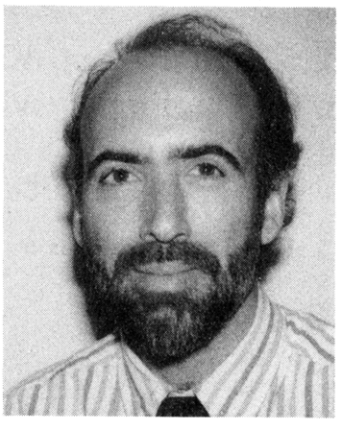

Paul M. Jones received his B.A. degree in both chemistry and mathematics at SUNY at Binghamton (Harpur College) in 1982 while working in the research group of Professor D. C. Doetschmann in the Department of Chemistry. He is currently an IBM fellow working toward the completion of his Ph.D. requirements at Stanford University in the research group of Professor Edward I. Solomon investigating the electronic structure of chemisorbed species on metal oxide single-crystal surfaces.

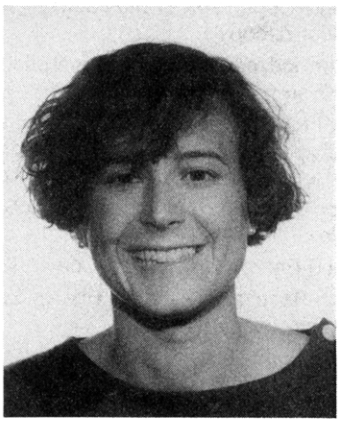

Jennifer A. May was born in Indianapolis, IN, in 1967. She received her B.S. degree with honors in chemistry from Brown University in 1989. Her undergraduate research was directed by Professor Eric Suuberg in the Department of Chemical Engineering. She is currently interested in the electronic structure of small molecules relevent to methanol synthesis chemisorbed on metal oxide single-crystal surfaces.

$CO/[Ni]_{surface}$ complex the stretching frequency is 2069 cm^{-1}; the gas-phase value of ν_{CO} is 2143 cm^{-1}. However, for CO binding to ZnO powders the CO stretching frequency is found to be at 2212 cm^{-1}, far above its gas-phase value.[13] This increase in the CO stretching frequency led to a variety of unusual proposals for the CO/ZnO surface complex including CO binding carbon end to the surface oxide forming a pseudo-CO_2 surface species and CO binding oxygen end down to the coordinatively unsaturated zinc ion.[14,15]

This unique inorganic complex also has an *unusual reactivity in catalysis*. Hydrogenation of CO on many metal surfaces (for example nickel in eq 1) results in the generation of methane while hydrogenation of CO on ZnO produces methanol where the C–O bond is retained in the product.[13] There are two promoters

$$CO + 3H_2 \xrightarrow{Ni} CH_4 + H_2O \quad (1)$$

$$CO + 2H_2 \xrightarrow[M_2O_3/Cu]{ZnO} CH_3OH \quad (2)$$

involved in this catalysis. M_2O_3 (where M = Cr or Al) is an intercrystalline promoter which when added in substoichiometric amounts forms the zinc chromite spinel structure which inhibits ZnO crystallites from sintering and losing surface area.[16,17] In these systems ZnO is the active phase in catalysis.[18] In the commercially used methanol synthesis catalyst, copper is added as an intracrystalline promoter which greatly reduces the activation barrier for catalysis (from 30 to 18 kcal/mol), allowing lower temperature and pressure reaction

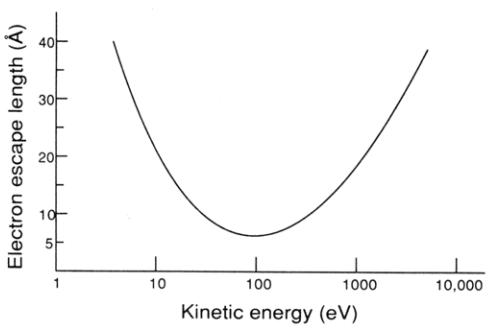

Figure 1. Escape depth curve. Average escape depth of an electron as a function of its kinetic energy. (Adapted from ref 6.)

conditions.[19] In the first half of this review we will consider the CO/ZnO system in some detail to define the geometric and electronic structure of the surface species involved in catalysis. In the second half of this review we focus on the nature of the copper-promotion effect in the commercial catalyst by studying the surface copper site on ZnO and its interaction with CO in order

Table I. Metal Oxide Catalysts

reaction	metal oxide	ref(s)
	Hydrogenation	
methanol synthesis	Cu/ZnO	136–140
	Oxidations	
oxidative coupling of methane	Bi/Mn–O	141
	Ba_2LaBiO_4	142
	La_2O_3, CeO_2, Sm_2O_3, Eu_2O_3, Yb_2O_3	143
	Li/MgO, Na/MgO, Li/CaO, Na/CaO, K/CaO, Li/La_2O_3	144
	Nb_2O_5 or ZrO_2 in Li/MgO and Li/Na/MgO	145
	La_2O_3/BaO	146
oxidative coupling of methylbenzenes	MoO_3, V_2O_5, Re_2O_7	147
oxidation of propene to acrolein (ammoxidation of propylene to acrylonitrile)	MoO_3/Sb_2O_4, $Bi_2Mo_3O_{12}$	147–151
oxidation of olefins	Bi_2MoO_6	152
oxidation of butene to maleic anhydride	$MnMoO_4$	153
	MoO_3/TiO_2	154
oxidation of toluene	VO_x/TiO_2	155,156
oxidation of hydrocarbons	Cr_2O_3	157
	NiO	158
oxidation of CO	$La_{1-x}Sr_xMnO_3$	159
	Reductions	
reduction of NO with NH_3	V_2O_5	160
reduction of NO to NH_3	$La_{1-x}K_xMnO_3$	161
	Polymerizations	
ethylene oxide polymerization	Al_2O_3, MgO, TiO_2	162
oligomerization of propylene	$Al_2O_3/SiO_2/MoO_3$, WO_3, UO_3, Cr_2O_3, NiO, FeO, ZnO	163,164
	Cracking	
cracking of *n*-heptane	CaO, MgO	165

Table II. Metal Oxide Surfaces and Their Interaction with Small Molecules, Studied with Electron Spectroscopy

metal oxide	small molecules	spectroscopy	observation	ref
MgO(100)	CHO_2H and CH_3CO_2H	HREELS	surface formate	166
MgO/Mo(100)	H_2O, CH_3OH	HREELS, LEED	hydroxide and methoxide	167
TiO_2(110)	H_2S	UPS	dissociative adsorption (low coverages), molecular adsorption (high coverages)	168
	O_2	UPS	dissociative adsorption	169
	H_2O	UPS	surface hydoxyl	170
	H_2	UPS	does not interact	171
$Ti_2O_3(10\bar{1}2)$	SO_2, CO	UPS, XPS, LEED	SO_2 oxidizes the surface, CO is dissociatively adsorbed	172
Ti_2O_3(047)	O_2	UPS, EELS	O^{2-}	173
	H_2O	UPS	dissociative adsorption of H_2O	174
$V_2O_3(10\bar{1}2)$	O_2, H_2O	XPS, UPS	O^{2-}, dissociative adsorption of H_2O	175
	SO_2	XPS, UPS	molecular and dissociative adsorption	176
Cr_2O_3(111)	CO, CO_2	EELS, LEED, ARUPS, NEXAFS, XPS	CO adsorbed parallel to the surface, CO_2 produces a surface carbonate	177
MnO(100)	O_2, CO, H_2O	UPS	dissociative adsorption of O_2, molecular adsorption of CO, deprotonation of H_2O	178
Fe_2O_3(0001)	O_2, H_2O, H_2, SO_2	UPS	O^{2-}, H_2O is dissociatively adsorbed, SO_2 yields a sulfate surface species	179
CoO(100)	O_2	resonant photoemission, UPS	O^{2-}	180
	CO, O_2, H_2O	UPS, AES, LEED	CO adsorption reduces the surface, H_2O is dissociatively adsorbed	181
NiO(100)	O_2, H_2O	UPS, XPS, LEED, Auger	O_2 adsorption at defect sites, H_2O is deprotonated	182
	NO	XPS, ARUPS, NEXAFS, HREELS	NO does not adsorb on defect sites	183
ZnO(0001)	CHO_2H	HREELS	surface formate	184
$SrTiO_3$(111)	O_2, H_2, H_2O	UPS, XPS	O^{2-} from O_2, surface hydroxyl from H_2, hydroxide from H_2O	185
$SrTiO_3$(100)	O_2	UPS	O^{2-}	169
	H_2O	UPS	molecularly chemisorbed	170

to define electronic structure differences relative to CO binding to pure ZnO which relate to differences in the efficiency of catalysis.

Finally, due to the wurzite structure of ZnO, the interaction of CO can be studied on four chemically different low index surfaces (Figure 2).[7,20] The polar surfaces (0001) and (000$\bar{1}$) contain only coordinatively unsaturated zinc or oxide ions, respectively, with the coordinatively unsaturated direction normal to the surface. The nonpolar (10$\bar{1}$0) and (11$\bar{2}$0) surfaces contain both coordinatively unsaturated zinc and oxide ions. For the (10$\bar{1}$0) surface these form dimer surface sites with the coordinatively unsaturated direction at 19° off the surface normal, while the (11$\bar{2}$0) surface has

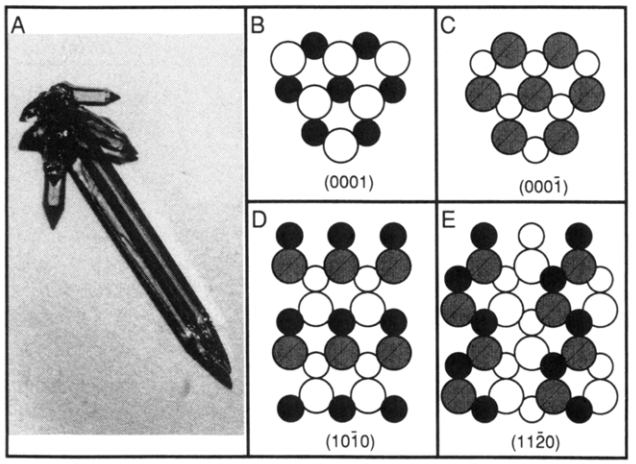

Figure 2. Zinc oxide crystal structures: (A) Single crystal of ZnO; (B–E) space-filling representations of the ideal low index ZnO surfaces as viewed from above with the darkened spheres representing surface ions, small spheres representing Zn^{2+}, and large spheres representing O^{2-}.

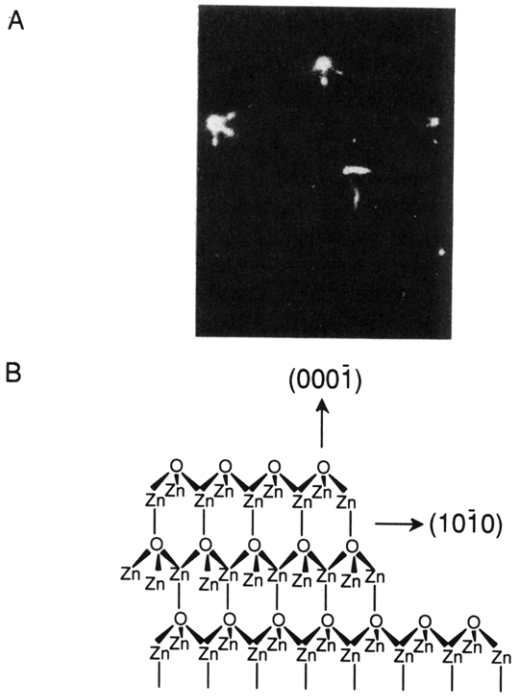

Figure 3. Structure of polar ZnO surfaces. Part A shows LEED pattern of ZnO(000$\bar{1}$). The streaks indicate two double layer surface steps in the (10$\bar{1}$0) direction as shown in B. Note that the coordinatively unsaturated direction on Zn^{2+} step sites is 70° off the surface normal.

zigzag chains with the unsaturated direction at 35° off the surface normal. These surfaces have been studied by low-energy electron diffraction (LEED).[21] No symmetry changing reconstruction is observed for any surface but dynamical analysis of the LEED spot intensities indicates that there is some relaxation of the zinc ions by a few tenths of an angstrom into the surface on both the (0001) and (10$\bar{1}$0) surfaces.[21,22] Streaking of the LEED patterns of the polar surfaces indicate that further refinement of the surface structures is required (Figure 3A). These streaks indicate that the polar surfaces (which are electrostatically unstable) form steps. Analysis[23,24] of the streaking for the oxide surface shows that this result is caused by a terrace of surface oxides with a two double layer, one unit cell step in the (10$\bar{1}$0) direction (Figure 3B). On these (000$\bar{1}$)-oxide surface steps, zinc ion sites are exposed which have coordinatively unsaturated directions at 70° off the surface normal. In the next section we define the electronic structure of these clean surfaces using variable-energy photoelectron spectroscopy.

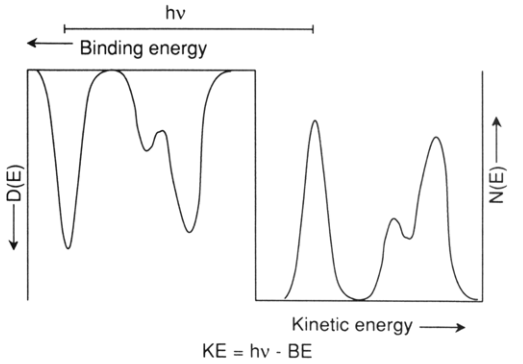

Figure 4. The photoelectron spectroscopy experiment. The density of states as a function of binding energy is correlated to the number of electron counts at a given kinetic energy.

II. The Electronic Structure of Clean ZnO Surfaces: Variable-Energy Photoelectron Spectroscopy

In photoelectron spectroscopy, photons with fixed energy impinge on a sample thereby ejecting electrons whose kinetic energies are analyzed using either a cylindrical mirror analyzer (CMA) or a hemispherical detector. The photon source can be a helium discharge (emitting He(I) photons at 21.2 eV or He(II) at 40.8 eV), an X-ray anode (Mg K_α at 1253.6 eV, Al K_α at 1486.7 eV), or a storage ring (emitting synchrotron radiation which is continuous over a wide range of photon energies). The kinetic energy (KE) of the ejected electron is equal to the input photon energy ($h\nu$) minus the binding energy (BE) of the electron to the sample. Thus as shown in Figure 4, scanning the spectrum to lower kinetic energy probes electrons in deeper binding energy orbitals. He(II) (40.8 eV) photons are often used to obtain a spectrum of the density of states of the valence band region of a sample. In this section we focus on the spectrum of "clean" ZnO surfaces which are prepared by orienting a crystal for the low index surface of interest (Figure 2) and then cutting, polishing, and acid etching the sample which is then placed on a manipulator in ultrahigh vacuum ($<10^{-10}$ torr). The surface is then sputtered with argon ions and annealed in cycles until it is clean by Auger electron spectroscopy and well formed by LEED.

The He(II) photoelectron spectra of the four surfaces of ZnO are shown in Figure 5. There are three broad peaks in the spectrum at 4, 7, and 11 eV binding energy referenced to the Fermi level (E_F) of ZnO. Initial insight into the assignment of these peaks is available from the results of a transition state, self-consistent field-Xα-scattered wave (SCF-Xα-SW) calculation on a tetrahedral ZnO_4^{-6} cluster which are included in Figure 5.[25,26] The lowest binding energy peak contains transitions from the 2e, $7t_2$, and $1t_1$ levels which involve the oxygen 2p orbitals that are only weakly π or nonbonding with the zinc ion. The peak in the 7-eV region has contributions from the $6a_1$ and $6t_2$ levels which involve oxygen 2p orbitals σ bonding to the unoccupied 4s and 4p

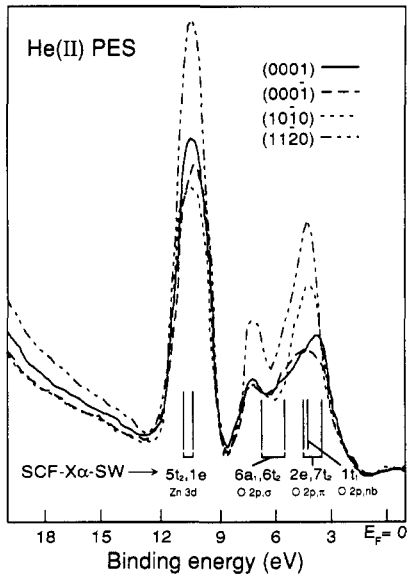

Figure 5. He(II) PES spectra of the valence band region of the four low index surfaces of ZnO. Fermi level (E_F) obtained from gold is defined as zero. Results from SCF-Xα-SW calculations are included.

orbitals of the zinc ion. Finally, the deepest binding energy peak is the zinc 3d band, and the t_2–e energy separation is the ligand field splitting of the d orbitals normally defined as 10Dq in crystal field theory. It is interesting to note that this splitting is in fact inverted (t_2 more stable than e) relative to the normal tetrahedral splitting in crystal field theory which derives from the fact that in the calculation the d band is at deeper binding energy relative to the oxide valence region and hence is involved in bonding interactions with the oxide orbitals. Normally in transition metal compounds the d band is at lower binding energy than the ligand valence orbitals and is antibonding. This assignment of the ZnO spectrum can be confirmed experimentally using variable-energy photoelectron spectroscopy.[26]

In this experiment the photon energy is scanned using synchrotron radiation, and the intensity of the photoelectron spectrum is measured as a function of input photon energy. From Figure 6A increasing the photon energy increases the kinetic energy (KE) of an electron ionized from a level at fixed binding energy. Since the deBroglie wavelength (in angstroms) of an electron is $12.3/[\mathrm{KE(eV)}]^{1/2}$, increasing the photon energy decreases the wavelength of the ejected electron and hence the overlap of the initial and final states. Quantitatively, the radial continuum wave function for the final state, ψ_f, is obtained by solving the radial Schrödinger equation; this produces a continuum wave function significantly modified relative to a free electron in the vicinity of the nucleus. The electric dipole intensity of a photoelectron peak is proportional to $\langle\psi_i|r|\psi_f(\mathrm{KE})\rangle^2$ which depends on both the final state kinetic energy of the ejected electron and the initial orbital from which the electron is ejected.[27,28] This will be different for an electron ionized from an oxygen 2p orbital as compared to one ionized from a zinc 3d orbital.[29] This intensity dependence on the initial-state orbital and final-state kinetic energy is known as the atomic photoionization cross section. From the theoretical cross sections in Figure 6C, the intensity of a peak corresponding to a 2p ionization is very large at photon energies near the ionization threshold and decreases with increasing photon energy. For an electron ionized from a 3d orbital, there is low intensity at low photon energy with a broad delayed maximum in photoelectron intensity peaking at an ~50 eV photon energy. This is caused by the repulsive centrifugal potential in the radial Schrödinger equation which is proportional to $\ell(\ell+1)$

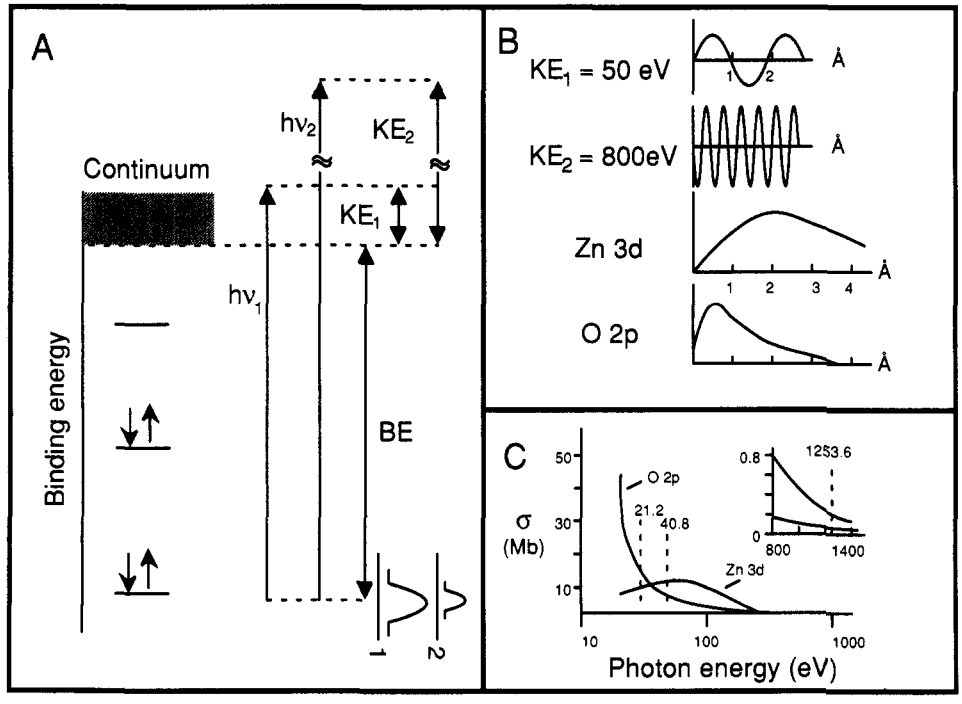

Figure 6. Photon energy dependence of the photoionization cross section: (A) The kinetic energy of the outgoing photoelectron increases with photon energy, $h\nu_2 > h\nu_1$, giving $KE_2 > KE_1$. (B) The different deBroglie wavelengths of the photoelectrons are compared to the radial wave functions of Zn 3d and O 2p orbitals. (C) Energy dependence of atomic photoionization cross section of Zn 3d and O 2p orbitals. Dashed lines indicate He(I), He(II), and Mg Kα sources. Insert gives high photon energy at higher sensitivity. 1 mb = 10^{-18} cm^2. (Adapted from ref 29.)

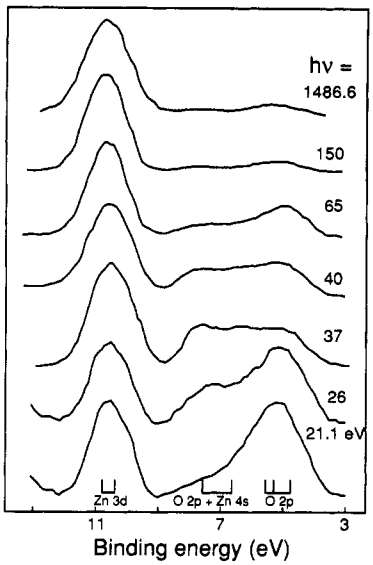

Figure 7. Variable-photon energy valence band PES data of ZnO, normalized to d band. SCF-Xα-SW assignments indicated at bottom.

where ℓ is the orbital angular momentum of the initial state.[30-33] This tends to keep the radial part of the continuum wave function small in the vicinity of the initial orbital wave function, resulting in limited overlap and thus low photoelectron intensity. As the kinetic energy of the photoelectron increases, the continuum wave function penetrates this centrifugal barrier resulting in better overlap with the initial state wave function and thus greater intensity.

The variable-energy photoelectron spectra of clean ZnO are given in Figure 7 (photon energy increasing from bottom to top).[25] The two low binding energy peaks are intense at low photon energy and decrease in intensity with increasing photon energy relative to the peak at 11 eV binding energy. From the theoretical cross sections in Figure 6C, the low binding energy peaks can be assigned as oxide photoemission and the peak at deeper binding energy (11 eV) as Zn 3d emission consistent with the SCF-Xα-SW calculations.[25] The Zn 3d band is at deep binding energy due to the high effective nuclear charge on the zinc ion. This difference in electronic structure relative to most transition metal complexes can have significant chemical consequences (vide infra). Finally it should be noted in Figure 7 that there are some quantitative differences in the intensity dependence on photon energy of the 4 and 7 eV peaks. This derives from the presence of Zn 4s character mixed into the O 2p peak at 7 eV and can be used to quantitate this covalent bonding as described in ref 26.

III. CO Chemisorption on ZnO Surfaces

A. He(II) Photoelectron Spectrum of CO on ZnO(10$\bar{1}$0)

Exposing the clean ZnO(10$\bar{1}$0)-dimer surface to a 10^{-6} torr ambient of CO at 90 K results in the appearance of new features in the photoelectron spectrum associated with chemisorbed CO (Figure 8, top).[7] The spectrum of the chemisorbed surface species can be estimated by subtracting off the clean ZnO substrate photoemission spectrum which must be attenuated due to surface CO coverage and shifted in energy to

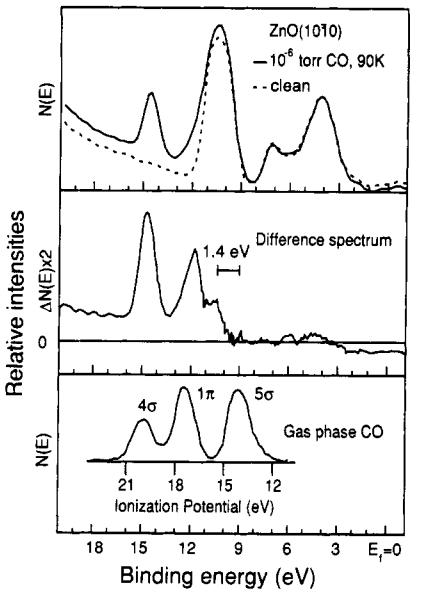

Figure 8. Interaction of CO with ZnO(10$\bar{1}$0) at 90 K: (Top) He(II) PES spectrum of the (10$\bar{1}$0) surface at 90 K before and after (solid line) exposure to a 10^{-6} torr ambient of CO (the clean spectrum has been attenuated and shifted to maximize overlap in the oxide region). (Middle) Difference between exposed and clean spectra. (Bottom) Photoelectron (35 eV) spectrum of gas-phase CO aligned to 4σ peak.

compensate for changes in band bending upon chemisorption. The difference spectrum of chemisorbed CO in Figure 8, middle, exhibits three peaks. These can be assigned by correlation to the gas-phase photoelectron spectrum of CO[14] taken at a similar photon energy (Figure 8, bottom) which has been aligned to the peak at deepest binding energy. This alignment corresponds to a 0.7 eV shift to lower binding energy relative to the vacuum level which is at 4.4 eV above the Fermi level of ZnO (vide infra). This extramolecular relaxation polarization shift (ERPS) of the spectrum derives from the fact that electrons of the ZnO substrate screen the chemisorbed CO photoemission process.[34,35] The deepest binding energy peak corresponds to electrons ionized from the 4σ molecular orbital which corresponds to the lone pair on the oxygen of CO. The 1π results from ionization from the CO π bond, and the 5σ peak at lowest binding energy corresponds to ionization from a molecular orbital which is largely a lone pair centered on the carbon.

The difference spectrum procedure described above is not completely rigorous in that it does not allow for changes in substrate photoemission due to changes in ZnO surface states.[36,37] Chemisorption depletes these surface states at the top edge of the oxide valence band (leading to a small dip in the difference spectrum) and sharpens the Zn 3d band. This affects the energy and shape of the lowest binding energy peak in the difference spectrum in Figure 8, middle. However, the data in Figure 8 clearly indicate that the 5σ peak has been stabilized to deeper binding energy relative to gas phase. Variable-energy photoelectron spectroscopy utilizing the cross-sectional differences of the CO 5σ relative to the Zn 3d photoemission process allows a reasonable estimate of the energy position of the 5σ level which corresponds to a 1.4 eV stabilization of this molecular orbital upon chemisorption to ZnO (10$\bar{1}$0).[38] A final feature to note from Figure 8 is that the 4σ peak is in

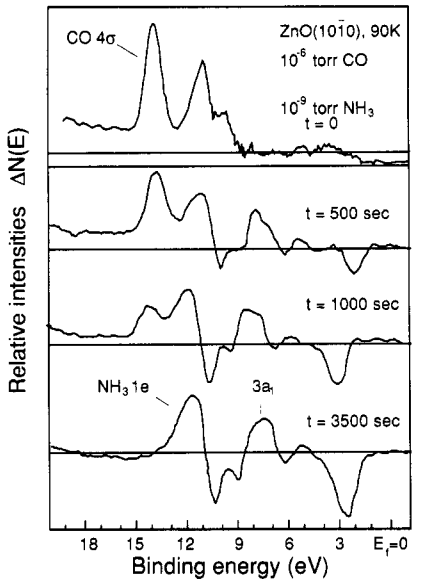

Figure 9. Competition of NH_3 with CO on ZnO(10$\bar{1}$0): Difference spectra for (10$\bar{1}$0) surface in 10^{-6} torr of CO at 90 K are shown upon increasing time exposures to 10^{-9} torr of NH_3. Key spectral features for dominant adspecies are indicated in top and bottom figures.

a spectral region which does not overlap the ZnO substrate photoemission and thus can be accurately used to probe chemisorbed CO on ZnO surfaces as described in the following sections.

B. Ammonia Competition in Ultrahigh Vacuum

Since the CO/ZnO surface complex is an unusual inorganic species, it is useful at this point to consider ammonia binding to ZnO, which is a more intuitive chemical system.[7,39] Ammonia is a Lewis base which should bind to coordinatively unsaturated zinc ion Lewis acid sites to form dative bonds. This is complicated by the presence of the surface oxide which can lead to deprotonation forming an inorganic amide. There has been some conflicting data from IR studies on powders as to whether this occurs on ZnO.[40,41] However, studies of NH_3 on single-crystal surfaces of ZnO at low temperature show that only nonreactive chemisorption occurs with a quite high heat of absorption (ΔH_0 = 28 kcal/mol) indicating a strong Zn(II)–NH_3 bond.[39]

One can then start with the CO/ZnO(10$\bar{1}$0) system described in section III.a (10^{-6} torr, 90 K) and add a small ambient of NH_3 (10^{-9} torr) and allow for a 3.5 langmuir exposure (1 langmuir = 10^{-6} torr s). From Figure 9 the 4σ peak of chemisorbed CO is eliminated, and the CO spectrum is replaced by the ammonia difference spectrum at the bottom of the figure. The 1e and $3a_1$ peaks correspond to chemisorbed NH_3, with the $3a_1$ stabilized by 2 eV relative to the gas-phase value.[7,42] This molecular orbital corresponds to the lone pair on the nitrogen, and the stabilization is associated with the strong ammonia σ-bonding interaction with the unoccupied 4s and 4p orbitals on the zinc ion.

The important point in Figure 9 is that NH_3 effectively competes with CO for binding to the ZnO surface. Since ammonia binds to zinc sites this indicates that the dominant bonding interaction of CO is also with the zinc ions which is confirmed in the next section. From the last section, the 4σ–5σ splitting is found to

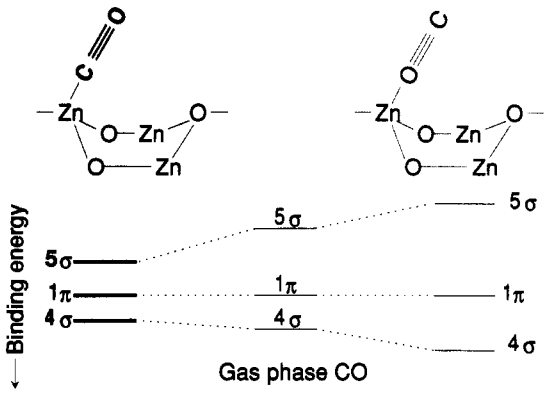

Figure 10. Possible CO binding geometries on ZnO(10$\bar{1}$0). Also included are the molecular orbital splitting patterns associated with each structure. Darkened part of figure indicates electronic and geometric structure consistent with experiment.

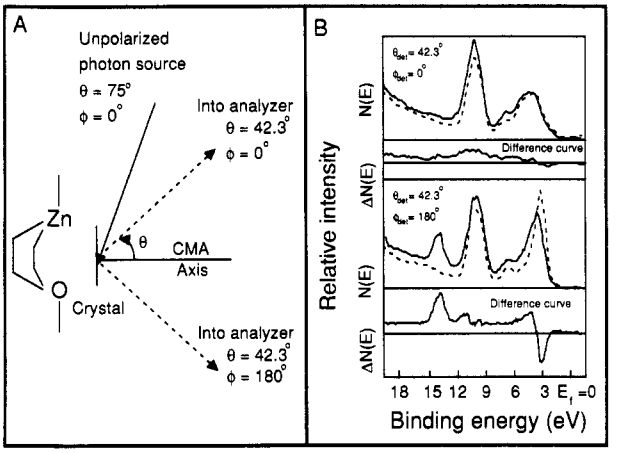

Figure 11. Crude angle-resolved PES of CO on ZnO(10$\bar{1}$0): (A) experimental configuration and (B) angle-resolved spectra and difference. For part B, crystal surface normal at θ = 5°, ϕ = 0°, and *c* at θ = 95°, ϕ = 0°. Clean (dashed line) and CO covered (solid line) spectra are shown for (top) θ = 42.3°, ϕ = 0° and (bottom) θ = 42.3°, ϕ = 180°. The spectra were taken at 90 K in a 10^{-6} torr ambient of CO.

decrease for CO binding to ZnO indicating that the 5σ orbital is stabilized due to bonding to the zinc ion, and thus CO binds carbon end down to the coordinatively unsaturated zinc site on the (10$\bar{1}$0) surface as illustrated in Figure 10, left.

C. Angle-Dependent Photoelectron Spectroscopy

It is possible to set up an experiment in a standard photoelectron spectrometer which confirms the general model for CO binding to ZnO(10$\bar{1}$0) presented on the left of Figure 10. Two points of background are required in order to understand the results of this experiment. First the coordinatively unsaturated direction of the zinc ion on the (10$\bar{1}$0) surface is tilted 19° off the surface normal toward the −*c* crystallographic direction. Second, as will be described in more detail in section IV the angular distribution of photoemitted electrons is highly anisotropic with the 4σ photoemission being primarily directed along the C–O molecular axis.[43] Thus one can start with the photoelectron chamber shown in Figure 11A, where the CMA detects electrons in a 6° cone 42.3° off the surface normal and mask off the CMA so that one detects either electrons emitted along the coordinatively unsaturated oxide direction (ϕ = 0°)

or along the coordinatively unsaturated zinc direction ($\phi = 180°$). From the spectra in Figure 11B, all CO 4σ intensity is observed for detection along the coordinatively unsaturated zinc direction as anticipated from the structure in Figure 10, left.[7] Note that in the experiment in Figure 11B the light source was not polarized.

D. Thermodynamics of Chemisorption on Four ZnO Surfaces

One can now extend the above study of CO chemisorption on the (10$\bar{1}$0) surface to the four chemically different surfaces in Figure 2 to probe the effects of the surface oxide and the different surface geometries on chemisorption. Figure 12 compares data for CO binding to the (0001)-zinc surface to those for the (10$\bar{1}$0)-dimer surface.[7] Clearly the CO 4σ intensity is lower on the zinc surface. However, it should be noted from Figure 12 that for a fixed ambient of CO the 4σ intensity is a function of temperature. This chemisorption process is in fact reversible, and in order to compare 4σ intensities it is necessary to develop the thermodynamics of CO binding to the four chemically different surfaces of ZnO.[7] Figure 13 presents the intensity of the 4σ peak as a function of temperature for two different ambient pressures of CO on the four low index surfaces of ZnO. The isosteric heat of adsorption ΔH_{ads} can then be determined from the Clausius–Clapeyron equation (eq 3):

$$[\partial \ln P/\partial(1/T)]_\theta = -(\Delta H_{ads}/R) \quad (3)$$

The heat of adsorption thus found on all of the chemically different surfaces indicates that ΔH_{ads} decreases with increasing coverage. For a well-formed single-crystal surface possessing homogeneous adsorption sites this decrease should be due to a repulsive dipole–dipole interaction and can be adequately described by the Temkin isobar expression[44] (eq 4):

$$\Delta H_{ads} = \Delta H_0(1 - \alpha\theta) \quad (4)$$

where α is a constant and ΔH_0 is the heat of adsorption at zero coverage. Thus

$$\theta/(1 - \theta) = kP \exp[\Delta H_0(1 - \alpha\theta)/RT] \quad (5)$$

where k is a proportionality constant of approximately 4.0×10^{-9}. Equation 5 can be solved iteratively to determine relative values of θ as a function of T at constant P. The fit to the data based on continuous variation in the heat of adsorption is quite good but does not preclude the possibility of surface heterogeneity. In either case, the heat of absorption at zero coverage is found to be 12 kcal/mol for all four surfaces indicating a similar bonding interaction with each surface. The key difference observed is in the 4σ intensity extrapolated to saturation coverage. It is highest on the two nonpolar surfaces, intermediate on the (0001)-zinc surface, and lowest but nonzero on the (000$\bar{1}$)-oxide surface. There are two factors which can contribute to these differences in 4σ intensity: the number of surface sites and the orientation of the CO molecule on the surface relative to the CMA collection geometry in Figure 11A. The thermodynamics indicate a similar bonding interaction with all four surface sites which should involve coordinatively unsaturated zinc ions on the basis of the (10$\bar{1}$0) results described above. Thus CO could be binding to terrace zinc sites on the (10$\bar{1}$0), (11$\bar{2}$0), and (0001) surfaces with the different

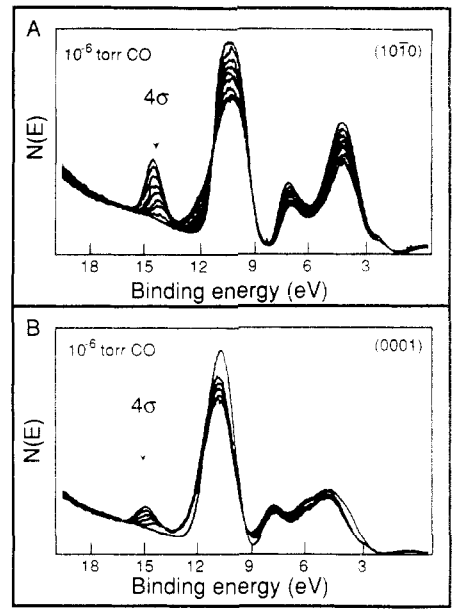

Figure 12. Chemisorption of CO on ZnO as a function of temperature: (A) ZnO(10$\bar{1}$0) and (B) ZnO(0001) in a 10^{-6} torr ambient as temperature is varied from 90 to 180K. The clean spectra have been included for comparison. Note that the 4σ intensity is decreasing with increasing temperature.

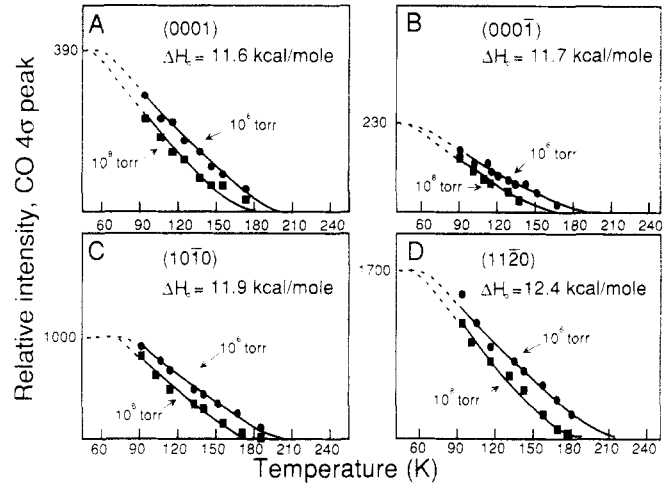

Figure 13. CO 4σ intensity as a function of temperature and pressure on (A) ZnO(0001), (B) (000$\bar{1}$), (C) (10$\bar{1}$0), and (D) (11$\bar{2}$0). Data has been fit to a Temkin isobar; extrapolated values are indicated with a dashed line. Data have been scaled to the relative intensities of the clean spectra and the size of the unit cell. Note that A and B are on a different scale from C and D.

4σ intensities in Figure 13 reflecting the different coordination unsaturation directions. Alternatively, for the (000$\bar{1}$) surface only terrace oxides are available. Thus the nonzero 4σ intensity for this surface could reflect CO binding to coordinatively unsaturated zinc sites on steps as described in Figure 3B. These possible CO/ZnO geometric structures were evaluated through detailed angle-resolved photoelectron spectral studies using polarized light as described in the next section.

IV. Geometric Structures for CO Binding to the Four Chemically Different Surfaces of ZnO: Angle-Resolved Photoelectron Spectroscopy

The angle-resolved photoelectron experiment is described in Figure 14A.[45] Polarized He(II) photons are

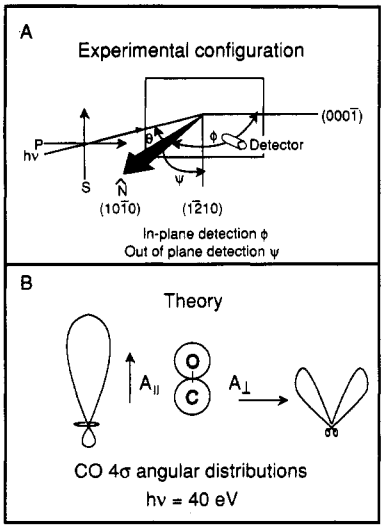

Figure 14. The polarized angle-resolved PES experiment: (A) ZnO(10$\bar{1}$0) experimental crystal orientation and (B) calculated angular distribution of electrons emitted from the 4σ orbital of CO with polarized 40 eV light. (Taken from ref 43.)

propagated into the surface with an angle of incidence θ relative to the surface normal. The polarization $\vec{A}$ vector of the light can either be oriented in the plane of incidence (P polarization) or perpendicular to the plane of incidence (S polarization). The electrons are then detected with a hemispherical detector which is scanned either in the plane of incidence (ϕ as in Figure 14A) or perpendicular to the plane of incidence (ψ). The angular behavior of the photoemitted electrons being probed in this experiment has been calculated by Davenport[43] and is given in Figure 14B which shows the angular distribution of electrons emitted from the 4σ molecular orbital of CO for 40-eV photons. There are two important features to note from these calculations. First, the maximum intensity is observed when both the $\vec{A}$ vector and the detector are along the molecular axis. Second, when the $\vec{A}$ vector of light is perpendicular to the molecular axis and the detector is in a plane perpendicular to the $\vec{A}$ vector but containing the molecule, there is a node in the 4σ photoemission intensity.

Focusing initially on the ZnO(10$\bar{1}$0) surface, the light is propragated at an angle θ of 70° off the surface normal along the c direction and the electrons were detected in the plane of incidence ϕ sweeping toward $-c$.[46] From the S-polarized data, Figure 15A, there is clearly a node in the 4σ intensity requiring that the CO molecule be perpendicular to the $\vec{A}$ vector and in the plane of incidence. The P-polarized data for the plane of incidence detection in Figure 15A show a peak in the 4σ-intensity distribution at an angle of about 30° toward the $-c$ direction which from Figure 14B is the approximate orientation of the CO molecular axis. A quantitative analysis was performed using the Davenport space-fixed, free-molecule calculations with corrections for the surface reflection of the electromagnetic wave and which also gave an angle for the orientation of the CO molecule of −30°.[46] The out-of-plane sweeps ψ in Figure 15B confirm that the molecule is in the plane of incidence and are quantitatively fit with the Davenport calculations using the same orientation as obtained from the in-plane sweeps in Figure 15A.

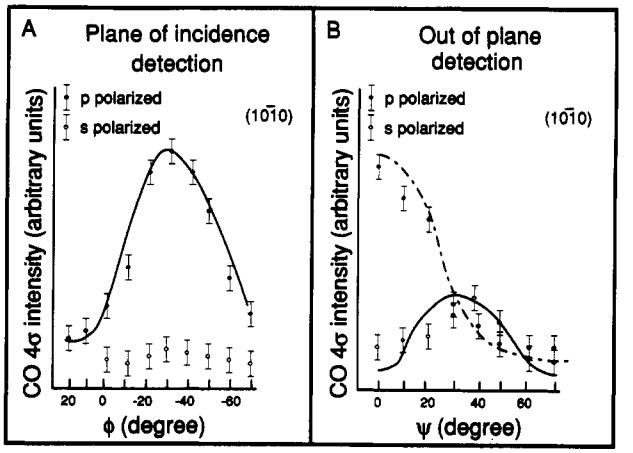

Figure 15. Angle dependence of CO 4σ intensity on ZnO-(10$\bar{1}$0): Photon angle of incidence is +70°: (A) plane of incidence detection with S and P polarized light and (B) out-of-plane detection with S and P polarized light. Solid and dashed lines in both are theoretical fit with Davenport expressions for CO tilted 30° off normal in the $-c$ direction.

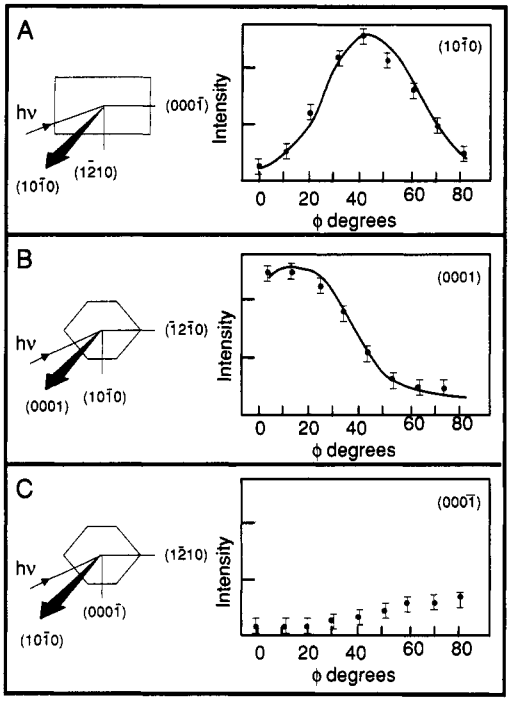

Figure 16. Angle-resolved PES studies of three chemically different surfaces of ZnO: Photoelectron angular distributions for the CO 4σ intensity in the plane of incidence for (A) (10$\bar{1}$0), (B) (0001), and (C) (000$\bar{1}$) surfaces. In each case the light is incident at 60° away from the surface normal and has P polarization. For all cases ϕ = 0° is the surface normal, and ϕ increases toward (A) (000$\bar{1}$), (B) (1$\bar{2}$10), and (C) (1$\bar{2}$10).

Figure 16 extends these angle-resolved photoelectron spectral studies over three chemically different surfaces of ZnO.[47] All three sets of data were taken with an angle of incidence of 60°, P polarization, and plane of incidence detection. The ZnO(10$\bar{1}$0) data in Figure 16A corresponds to the solid data points in Figure 15A. The small difference between the angle of incidence used in each of these experiments produces a slight change in the intensity distribution. However, the best fit to the data points in Figure 16A also gives a CO orientation of 30° off the surface normal toward the $-c$ direction on the (10$\bar{1}$0)-dimer surface. Figure 16B presents analogous data for the (0001)-zinc surface. Importantly,

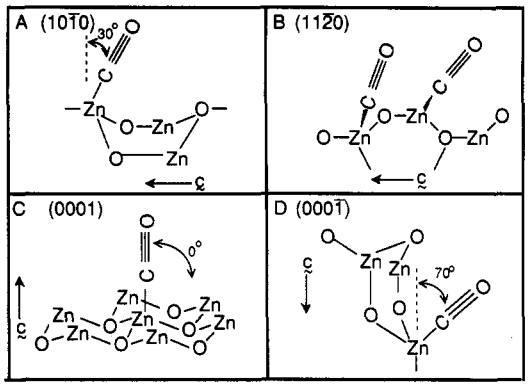

Figure 17. Geometric structures for CO binding on the four low index surfaces of ZnO. The angle given indicates the experimental CO orientation relative to the surface normal.

the peak in the intensity distribution is now shifted toward the surface normal, and the data is quantitatively fit to give a CO molecule binding normal to the surface.[47,48] Finally, the data in Figure 16C is for the (000$\bar{1}$)-oxide surface which is symmetrically equivalent to the (0001)-zinc surface yet the intensity detected at the surface normal is minimal and increases as one scans away from the normal.[47] A quantitative fit to this data gives a CO angle of ~70° off the (000$\bar{1}$) surface normal.

The data in Figures 15 and 16 provide a detailed picture of the geometric structures of the CO/ZnO surface complexes for the four low index surfaces of ZnO as shown in Figure 17. For the (000$\bar{1}$)-oxide surface the 70° angle confirms the possibility that CO binds to the coordinatively unsaturated zinc ions on step-sites.[49] For the (0001)-zinc surface CO binds along the surface normal, while for the (10$\bar{1}$0)-dimer surface CO binds at an angle of 30° off the surface normal. Since the open coordination position on the idealized surface is 19° off the normal, this could indicate some interaction with the surface oxide. However, the heat of absorption on this surface is, within error, the same as for the (0001) surface, thus any interaction with the oxide must be quite weak. The tilt could alternatively derive from the relaxation of the position of the zinc ion on this surface (vide supra).

Having obtained an accurate description of the geometric structure of CO binding to the zinc oxide surfaces, one can now probe the electronic structure of the CO/ZnO surface complex as described in the next section.

V. Electronic Structure of the CO/ZnO Surface Complex

A. He(I) Energy Distribution Curves (EDC)

As illustrated in Figure 18A, in addition to the primary photoelectrons of the ZnO substrate, the He(I) photoelectron spectrum contains a tail to deeper binding energy due to inelastically scattered secondary electrons. The composite EDC for clean ZnO is given by the dashed spectrum in Figure 18B. The onset of the inelastic tail corresponds to electrons escaping from the substrate with zero kinetic energy.[4] Therefore 21.2 eV (the He(I) photon energy) above this onset is the vacuum level. The Fermi level is obtained by taking a spectrum of a gold sample which is in electrical contact with the ZnO crystal. The difference between the Fermi level and the He(I) defined vacuum level then gives the

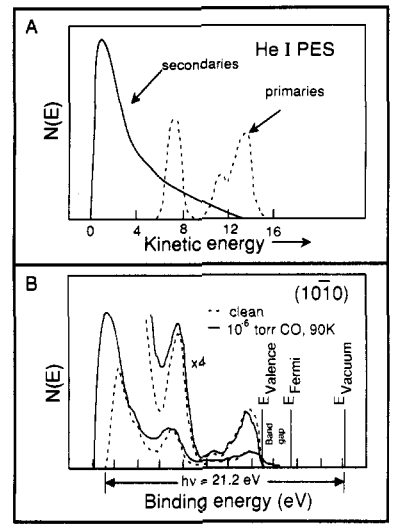

Figure 18. He(I) energy distribution curves: (A) (solid) secondary electron tail, (dashed) primary photoelectron spectrum; (B) experimental composite EDC for clean ZnO (dashed line) and ZnO in 10^{-6} torr CO ambient at 90 K (solid line). Top edge of the valence band ($E_{valence}$), Fermi level (E_{Fermi}), and vacuum level (E_{vacuum}) are indicated.

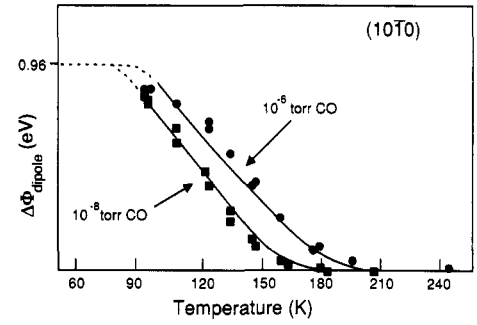

Figure 19. Dipole contribution to work function. The dipole contribution to the work function for ZnO(10$\bar{1}$0) varies as a function of temperature and pressure. Solid lines are fit using same Temkin expression as in Figure 13; extrapolated values of fit are indicated with dashed line.

work function which can be studied as a function of CO chemisorption. For an n-type semiconductor, such as ZnO, changes in the total work function, $\Delta\Phi_{total}$, are related to the build up of a dipolar layer ($\Delta\Phi_{dipole}$) and to the presence of surface electronic states induced by chemisorption which cause a rigid shift in the energy of the electronic band structure relative to the Fermi level ($\Delta\Phi_{bb}$) by eq 6.[2,3,7]

$$\Delta\Phi_{total} = \Delta\Phi_{dipole} + \Delta\Phi_{bb} \quad (6)$$

From Figure 18B, dashed to solid spectrum, the inelastic tail shifts to deeper binding energy with increasing CO coverage relative to a fixed Fermi level. Therefore the work function has decreased indicating that net negative charge is donated to the ZnO surface upon CO binding. The shift in the top edge of the valence band ($E_{valence}$) with CO coverage gives the change in band bending which can be subtracted from the total work function change to obtain the surface dipole contribution to the work function. Figure 19 gives the temperature and CO pressure dependence of the dipole contribution to the work function for the ZnO(10$\bar{1}$0) surface which is fit with the same thermodynamic expression used for the 4σ intensity in Figure 13. This gives the dipole contribution to the work function for a known surface

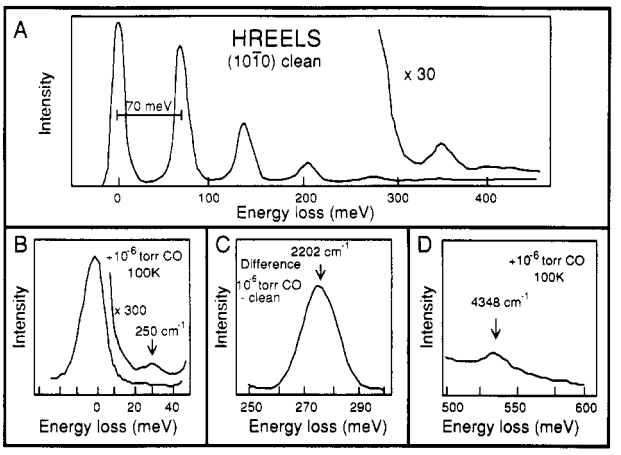

Figure 20. HREELS of CO on ZnO(10$\bar{1}$0): Part A shows the spectrum of the clean ZnO(10$\bar{1}$0) surface at T = 100 K taken with KE = ~4.5 eV. The features at ~70 meV intervals are due to multiple excitations of the Fuchs–Kliewer surface phonons (ref 52). Parts B–D show spectra of 10^{-6} torr CO, 100 K. Note that C is given as a difference spectrum (exposed minus clean) to eliminate contributions due to the surface phonon.

coverage. Further, knowing the coordination geometry of the surface complex and assuming no lateral interactions at these coverages, one can use the Hemholtz equation[51] (eq 7) to obtain an estimate of the Zn(II)–CO surface dipole moment, μ:

$$\mu = \Delta\Phi_{dipole}/(4\pi N_s\theta \cos\beta) \quad (7)$$

In eq 7 N_s is the number of surface sites per squared centimeter, θ is the fractional surface coverage and is available from the thermodynamic studies in section III.D, and β is the angle between the surface complex and surface normal which was found to be 30° in section IV. By using eq 7, the dipole moment of the CO/ZnO surface complex is found to be 0.61 D negative side toward the surface.

B. High-Resolution Electron Energy Loss Spectroscopy (HREELS)

The next feature of the electronic structure of the CO/ZnO surface complex relates to the IR vibrational studies on powders mentioned earlier. At this point it is important to confirm that this surface species exhibits the high CO stretching frequency found on ZnO powders and to use the vibrational data to further probe the CO bonding of the CO/ZnO surface complex. This was accomplished on the ZnO single-crystal surface using HREELS. In this experiment a low-energy (~4.5 eV) beam of monochromatic electrons is scattered off the surface and exhibits inelastic losses due to excitation of surface vibrations. The HREELS spectrum of clean ZnO (Figure 20, top) shows an intense 70 meV loss progression corresponding to multiple excitations of a surface optical phonon.[52–55] Exposure of this surface to an ambient of CO at low temperature results in the appearance of additional vibrational features associated with chemisorbed CO (Figure 20, bottom).[56] The first C–O overtone is observed at 539 meV (4348 cm^{-1}), the CO fundamental at 273 meV (2202 cm^{-1}), and the metal–ligand stretch at 31 meV (250 cm^{-1}). Therefore, this CO/ZnO surface complex does exhibit the high-energy CO vibration observed on powders. Further determining the metal–ligand stretching frequency enables one to perform a normal coordinate analysis of the surface complex to quantify the CO bonding. This is important since CO binding to a metal site leads to mechanical coupling between the metal–carbon and C–O stretch which will increase the CO stretching frequency. Therefore when the CO stretching frequency decreases upon binding to metals, this requires a decrease in the strength of the CO bond. In the normal coordinate analysis this manifests itself as a decrease in the CO stretching force constant (k_{CO}) relative to the gas phase value[57] (see Table III for Ni, etc.). Alternatively, if one uses the CO/ZnO vibrational data in Figure 20, the CO force constant is found to *increase* from 18.6 to 19.2 mdyn/Å upon chemisorption. The normal coordinate analysis shows that only 12 cm^{-1} of the 60 cm^{-1} increase in CO stretching frequency derives from vibrational coupling to the surface. Thus in contrast to the behavior on most metals[9,58–60] the CO bond has become stronger upon chemisorption to surface zinc ion sites.

C. Near-Edge X-ray Absorption Fine Structure (NEXAFS)

Evidence of increased CO bond strength upon chemisorption to ZnO is also found in the carbon K edge NEXAFS spectrum (Figure 21). This spectrum is obtained with reasonable surface sensitivity by detecting the intensity of the carbon KVV Auger electrons emitted as a function of photon energy when scanned through the carbon K edge.[38] The peak at 280 eV corresponds to the C 1s → CO 2π* transition while the feature at 310 eV is a σ-shape resonance. The latter is associated with lower energy states of the continuum which have wave functions localized within the CO molecule due to the interaction of the photoelectron with the potential of the atoms.[61] This produces significant overlap with the C 1s orbital leading to a relatively intense sharp transition in the low-energy region of the carbon edge continuum. The energy of this shape resonance is thus affected by the intramolecular C–O bond length.[62,63] Stöhr et al.[64,65] have developed a semiempirical equation based on multiple scattering theory to relate the resonance energy and the bond length, $(\delta - V_0)r^2 = C_0$, where δ is the energy difference between the shape resonance and the C 1s core level, r is the intramolecular bond length, and C_0 and V_0 are constants, equal to 35.7 ± 2.3 eV Å^2 and −9.2

Table III. Stretching Frequencies and Calculated Force Constants for Adsorbed and Gas-Phase CO

		ν_{M-C}		ν_{CO}		calculated	
surface	structure	meV	cm^{-1}	meV	cm^{-1}	k_{M-C} (mD/Å)	k_{CO} (mD/Å)
Pt(111)	C(4×2)	60	484	261	2105	4.19	16.41
Cu(100)	C(2×2)	43	347	260	2097	2.02	17.05
Ni(100)	C(2×2)	59.5	480	256.5	2069	3.98	15.87
ZnO(10$\bar{1}$0)		31 ± 1	250	273 ± 2	2202	1.01	19.21
gas phase				265.7	2143		18.56

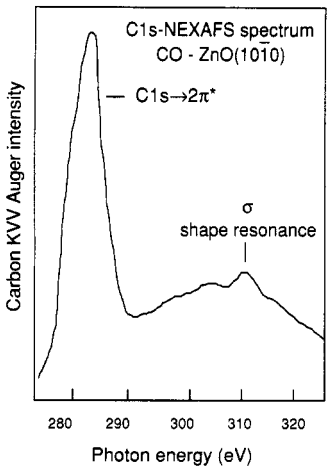

Figure 21. C1s-NEXAFS spectrum of CO/ZnO(10$\bar{1}$0) taken at 80 K with 9000 langmuir CO exposure. Note that the feature between 300 and 305 eV is due to the O 2s which is located ~27 eV below the Fermi level.

± 1.6 eV, respectively.[63] On the basis of the energy positions of the shape resonance in Figure 21 and of the C 1s XPS peak energy (vide infra), δ = 19.9 ± 0.5 eV and the C–O bond length for carbon monoxide chemisorbed on the ZnO (10$\bar{1}$0) surface is calculated to be 1.10 ± 0.05 Å. On the basis of the above equation, as the bond length of the chemisorbed species decreases, δ will increase though determination of the resulting bond length will be subject to some error. If the bond length of the chemisorbed CO were at its gas-phase value of 1.13 Å, the above formalism would predict a value of δ of 18.9 eV. For CO/Cu(110) where the CO bond length should be very close to the gas-phase value, the experimental δ is 18.8 ± 0.5 eV.[63] The larger experimental value of δ of 19.9 eV requires that the CO bond length has measurably decreased from its gas-phase value upon CO chemisorption to ZnO(10$\bar{1}$0). In contrast, for metal surfaces were the chemisorbed CO bond has weakened based on HREELS data δ is found to significantly decrease from 18.8 eV (e.g., for CO/Pt(111) δ is 17.3 ± 0.5 eV[66] and for CO/Ni(100) δ is 17.2 ± 0.5 eV[62]).

D. Geometric and Electronic Structure of the CO/ZnO Active-Site Complex

From the studies summarized above, CO binds carbon end down to the coordinatively unsaturated zinc ion. It acts as a σ donor stabilizing the 5σ molecular orbital to 1.4 eV deeper binding energy in Figure 8 and donating electron density to the surface. This leads to the net dipole moment of 0.61 D with positive charge on the carbon, and takes electron density out of the 5σ molecular orbital which is weakly antibonding with respect to the CO bond. Thus the CO bond in the CO/ZnO surface complex is shorter (from NEXAFS) and stronger (from HREELS) relative to the gas phase. Unlike CO bonding to most metals, there is no evidence for π backbonding for the CO/ZnO complex which is due to the high effective nuclear charge on the Zn(II) ion which contracts the orbitals and stabilizes the d band to deeper binding energy (Figure 5). This description of the CO/ZnO surface complex is summarized in Figure 22.

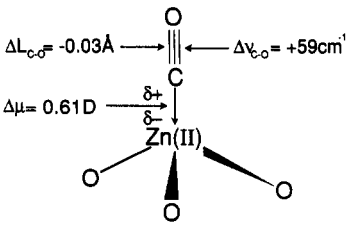

Figure 22. CO/ZnO active-site complex.

VI. Nature of Copper Sites on ZnO Surfaces

The copper component of the binary catalyst has received a great deal of attention due to its role as the promoter of the low-temperature, low-pressure methanol synthesis reaction.[18,67–71] Various workers have studied the catalyst derived from different precursors. Calcination (heat treatment) of the binary catalyst has been shown, by XPS and other probes, to oxidize the copper component to Cu(II).[72–74] A variety of physical methods have been used to probe the phase, dispersion, and oxidation state(s) of the copper in the active (reduced) catalyst. In an early study, Klier and coworkers probed the active binary catalyst with diffuse optical reflectance spectroscopy[18,68] and found a feature at 2.17 eV which was assigned as arising from a Cu(I) (3d) → ZnO (4s) conduction band transition with the cuprous ion substituted for Zn(II) in the lattice. A later XPS study[75] of coprecipitated reduced catalysts showed the presence of three copper species, depending on the copper concentration in the catalyst: a Cu(I) species at lower copper concentrations, copper clusters, and at higher copper concentrations a two-dimensional epitaxial monolayer over ZnO. More recently, frontal chromatography[76–78] using the decomposition reaction of N_2O with metallic copper has established a correlation between copper surface area and catalyst activity, thus leading to the proposal that copper in the form of small crystallites is the sole catalytic material in the binary catalyst,[79] with the support playing little or no role. Alternatively, other researchers believe that copper in intimate contact with the support is necessary for enhanced catalytic activity.[76,80] Finally, a recent theoretical study using the semiempirical quantum-mechanical formalism, INDO, on large Cu-doped ZnO clusters has assigned the copper oxidation state in the lattice as Cu(II).[81] Thus metallic copper, Cu(I), and Cu(II) sites on ZnO have all been proposed to be the active phase in the methanol synthesis catalyst.

A. Coordination Chemistry of Cu on ZnO Single-Crystal Surfaces

In order to investigate the nature of copper promotion of ZnO in the low-temperature, low-pressure methanol synthesis catalyst, the coordination chemistry of copper overlayers on the four chemically different single-crystal surfaces of ZnO has been investigated.[82] At room temperature and low copper evaporation conditions the first monolayer (ML) appears to grow in a two-dimensional fashion with low coverage copper existing as isolated centers and small islands on all surfaces. Large differences are observed in the coordination chemistry of the submonolayer copper sites on the

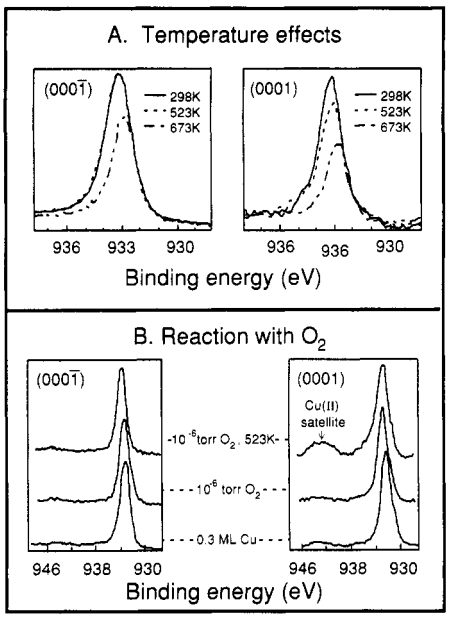

Figure 23. Cu $2p_{3/2}$ XPS studies of the effects of perturbations on 0.3 ML Cu on ZnO(000$\bar{1}$) (left) and (0001) (right) surfaces: (A) annealing to 298, 523, and 673 K; and (B) reaction with O_2 under conditions indicated.

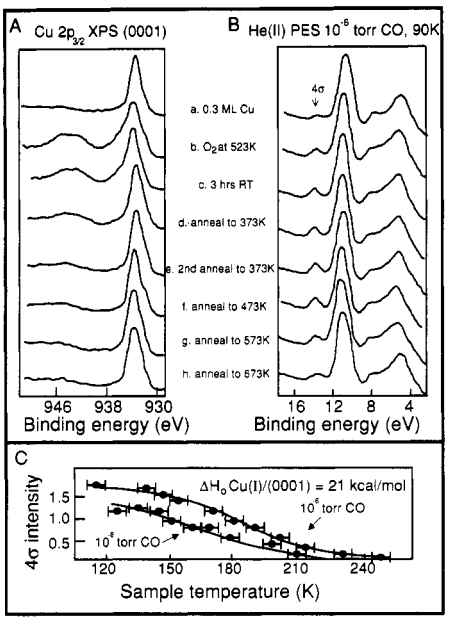

Figure 24. Chemisorption of CO on 0.3 ML Cu/ZnO(0001) surface: (A) Cu $2p_{3/2}$ XPS and (B) the He(II) valence band spectra at 130K in 10^{-6} torr of CO for surfaces obtained at the indicated conditions; (C) plot of the CO 4σ intensity on the oxidized Cu/(0001) surface (0.3 ML Cu, two anneals to 373 K) as a function of temperature and pressure.

chemically different surfaces which is illustrated using Cu $2p_{3/2}$ XPS data comparing 0.3 ML Cu on the (0001)-zinc and (000$\bar{1}$)-oxide surfaces in Figure 23. From Figure 23A, heating to reaction conditions (523 K) results in no observed change for 0.3 ML Cu on the (000$\bar{1}$)-oxide surface, while for copper on the (0001)-zinc surface the XPS peak is found to decrease in intensity and shift to lower binding energy. This decrease in intensity is not due to loss of copper from the surface but reflects its aggregation into larger islands with the shift to lower binding energy corresponding to increased extra-atomic final state relaxation in the larger clusters.[83] Further the submonolayer copper sites are found to be relatively unreactive on the oxide as compared to the zinc surfaces. Exposure to a 10^{-6} torr ambient of O_2 even at elevated temperatures produces little change in the Cu $2p_{3/2}$ XPS peak on the oxide surface (Figure 23B). Alternatively, for submonolayer copper on the zinc surface of zinc oxide a shake-up satellite peak appears on oxidation at 12 eV deeper binding energy from the Cu $2p_{3/2}$ primary peak. This is characteristic of the Cu(II) oxidation state indicating that the copper has been extensively oxidized on this surface.[84] This oxidation process can be quantified from the intensity ratio of the satellite to the main peak by referencing to analogous data on cupric oxide.[85] The data in Figure 23B, right, indicate that the submonolayer copper has been oxidized to 55% Cu(II) on the (0001)-zinc surface. Therefore, submonolayer copper on the oxide surface of zinc oxide appears to be more stable to the above perturbations perhaps reflecting a stronger Cu–ZnO bond with the oxide donor surface. Alternatively, the copper site could be physically blocked on this surface. For copper on the (0001)-zinc surface, the coordination chemistry described above allows one to prepare a variety of copper surface sites on ZnO including isolated centers, small and large clusters, Cu(I) and Cu(II) sites. The CO chemisorption properties of these sites have been studied in some detail as summarized in the next section.

B. Chemisorption of CO on Cu/ZnO Surface Sites

Figure 24A presents the Cu 2p XPS data for submonolayer copper deposited on the (0001)-zinc surface of ZnO which has been oxidized to the 55% Cu(II) level as described in the last section and then systematically reduced by limited heating in ultra high vacuum. This leads first to mostly Cu(I) surface sites (spectrum e) and eventually to aggregated copper metal (spectrum h). When these surfaces are cooled to 130 K and exposed to a 10^{-6} torr ambient of CO, the He(II) photoelectron spectra presented in Figure 24B, are obtained. Some CO 4σ intensity is observed in spectrum a associated with CO binding to the submonolayer copper as deposited. Oxidation to the 55% Cu(II) surface in spectrum b increases the CO 4σ intensity by 60%. This 4σ intensity increases further upon reduction, to twice the original oxidized surface intensity in spectrum b indicating that all 4σ intensity on the oxidized surfaces is due to CO binding to Cu(I) sites. Further reduction to Cu(0) and aggregation (spectra f–h) reduces the chemisorbed CO 4σ intensity. For the same number of copper sites these differences in CO 4σ intensity at fixed temperature and pressure should reflect differences in heat of adsorption, thus the 4σ intensity was studied as a function of temperature and pressure to obtain the thermodynamics for CO binding to the different copper sites on the ZnO surfaces. Figure 24C shows the data for the 4σ intensity for CO binding to the Cu(I) sites on the (0001)-zinc surface of ZnO. These data give a ΔH_0 for Cu(I)/ZnO(0001) of 21 kcal/mol. This is the highest value observed for CO binding to any site on all ZnO surfaces. For submonolayer Cu(0) on the ZnO(0001)-zinc surface, ΔH_0 is found to be 15 kcal/mol, equivalent to that for copper metal.[86] Alternatively, for submonolayer copper on the ZnO-(000$\bar{1}$)-oxide surface, no measurable 4σ intensity was

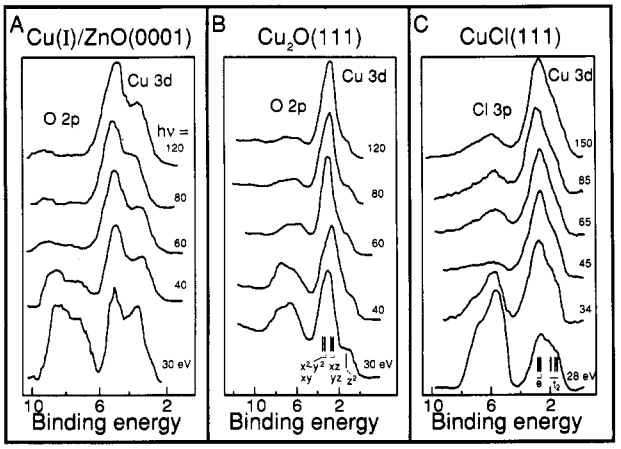

Figure 25. Variable-energy PES spectra of (A) 0.3 ML Cu/ZnO(0001) heated in 10^{-6} torr O_2 at 523 K minus clean ZnO at same photon energy (B) clean $Cu_2O(111)$, and (C) CuCl-(111). Ligand field splittings of the Cu_2O and CuCl d bands are included in bottom spectra of B and C.

observed,[87] indicating a ΔH_0 significantly less than that for binding to Zn(II) sites on clean ZnO surfaces (12 kcal/mol).

It is important at this point to relate the above results to those of Klier et al.[18] for CO binding to powders of the Cu/ZnO binary catalyst. These authors found that the presence of a high affinity CO binding site correlates with the catalytic activity. Therefore, on the basis of the heats of adsorption obtained above for well-defined copper sites on the chemically different surfaces of ZnO, *one can correlate this high affinity CO binding site with Cu(I) centers on the ZnO(0001)-zinc (and (10$\bar{1}$0)-dimer, see ref 82) surface.*

C. Nature of the Cu(I) Site on ZnO(0001) and Its Presence in Binary Cu/ZnO Catalysts

Variable-energy photoelectron spectroscopy has been used to probe the nature of the Cu(I) site on the ZnO-(0001) surface.[82] The spectra in Figure 25A were obtained by subtraction of the clean ZnO (0001) spectrum from that of the 0.3 ML oxidized Cu(I)/ZnO-(0001) spectrum at the same photon energy. Two sets of bands are observed; from their cross-sectional behavior[29] (the deeper binding energy band decaying in intensity with increasing photon energy) they are assigned as the oxide band (8 eV) and the ligand field split d band (4 eV). The relative intensities of the bands give a stoichiometry of approximately two copper atoms per one oxide which is correct for oxidation to Cu(I), but the d band splitting is not consistent with a Cu_2O (linear) structure. Shown in Figure 25B are the variable energy PES spectra of Cu_2O which exhibit a weak low binding energy peak in the d band (at 1.5 eV) that corresponds to the photoionization of a d_{z^2} electron.[89] The d_{z^2} orbital is at a high energy due to the linear two coordinate O–Cu(I)–O geometry of cuprous oxide. However, the d band splitting of Cu(I)/ZnO(0001) as seen in Figure 25A, with two peaks of comparable intensity at low photon energy does parallel that of CuCl in Figure 25C,[26,90] where the Cu(I) sites have tetrahedral geometries producing a t_2–e splitting of the d band of the d^{10} ion. The t_2 levels at lower binding energy are more dispersed and have more ligand cross

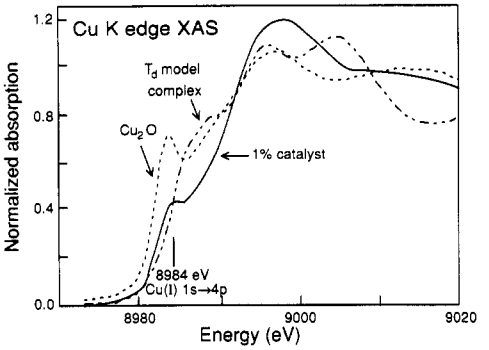

Figure 26. Cu K edge XAS of a Cu/ZnO catalyst. Normalized difference Cu K edge spectrum of the reduced 1% Cu catalyst, where the contributions of metallic Cu and Cu microclusters have been subtracted out. The normalized edges of Cu_2O (dashed line) and a 4-coordinate Cu(I) model, Cu[N(CH_2-CH_2-2-pyridyl)$_3$]BPh_4 (dot–dash) are included for comparison.

section character due to their strong σ antibonding interaction with the ligands. For the CuCl(111) surface the copper sites have open coordination positions normal to the surface leading to a further C_{3v} splitting of the t_2 band. Thus the ligand field splitting of the d band for the Cu(I)/ZnO(0001) system in Figure 25A strongly supports the presence of C_{3v} coordinatively unsaturated tetrahedral Cu(I) sites on this surface as pictured in Figure 26. It should be noted that Cox et al.[86] have recently studied the heat of adsorption of CO on $Cu_2O(100)$. They observed a ΔH_0 of approximately 17 kcal/mol which is higher than that found for copper metal, but lower than the 21 kcal/mol we find for Cu(I) in a C_{3v} coordinatively unsaturated site on the ZnO surface. This result parallels the trend observed by Sorrell and co-workers[91,92] for the reactivity of two versus three-coordinate Cu(I) model complexes with CO.

The possibility of tetrahedral Cu(I) sites being present in the Cu/ZnO binary catalysts has been probed using a combination of X-ray absorption spectroscopy (XAS) and extended X-ray absorption fine structure (EXAFS).[73,93] Analysis of the EXAFS spectra of the reduced (active) catalysts with different copper percentages has shown that there are four copper phases present: bulk metal, Cu_2O, small Cu microclusters, and Cu doped into the ZnO lattice. From the analysis of the ratio of the outer-shell EXAFS amplitude of the catalyst to that of copper foil, an estimate of the metallic copper present of ~15% was made for the 1% and 5% copper/ZnO catalysts. Subtracting off the metallic copper EXAFS results in a residual Cu–Cu feature at ~2.51–2.52 Å[73] which is indicative of Cu microclusters and corresponds to an effective cluster diameter of ~8 Å.[98] The percentage of total Cu present as 8-Å microclusters in the active catalyst was calculated to be ~20%. The remaining ~65% of the copper involves a Cu(I) oxide phase. The X-ray edges associated with this oxide phase for the reduced catalyst are given in Figure 26, which also presents the edge spectrum of Cu_2O and that of a tetrahedral Cu(I) model complex. The peak at 8984 eV observed in the reduced catalyst and Cu_2O is due to the Cu 1s → 4p transition. From our earlier studies,[99,100] the energy of this transition was found to depend on the geometry of the ligand field. Cu_2O has a linear ligand field at the copper which raises the $4p_z$ orbital energy due to the repulsive interaction along the ligand–metal bonds. Thus the 1s → $4p_{x,y}$ transitions

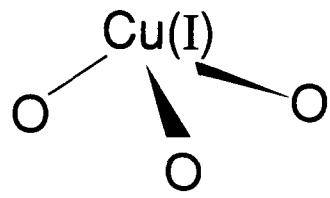

Figure 27. C_{3v} coordinatively unsaturated tetrahedral site for Cu(I) on ZnO(0001).

are at low energy and can be assigned to the 8984 eV peak on the basis of the polarized edge data on a linear Cu(I) model complex. Alternatively, in a tetrahedral ligand field all 4p orbitals experience a repulsive interaction and are raised in energy; therefore there is no low-energy 8984 eV peak in the spectrum of tetrahedral Cu(I) models complexes.[73,99,100] As shown in Figure 26, the normalized Cu(I) edge of the 1% Cu/ZnO catalyst in the 8984 eV region is clearly much weaker than that of the Cu_2O. On the basis of the intensity of this peak in the catalyst it is estimated that the oxide phase contains ~45% Cu(I) doped into tetrahedral sites in the ZnO lattice and ~20% Cu_2O.

Thus Cu(I) sites on the ZnO(0001) (and (10$\bar{1}$0), see ref 82) surface have been shown to bind CO with high affinity as has been observed for active catalysts and involve a coordinatively unsaturated tetrahedral Cu(I) site which is also present in the reduced binary catalyst (Figure 27). We now consider the electronic structure differences between CO binding to Cu(I) and Zn(II) sites which could contribute to the differences in reactivity associated with intracrystalline promotion.

VII. Electronic Structures of CO Bonding to d^{10} Metal Ion Sites

A. Molecular Orbital Considerations

There are two main contributions to CO bonding to a metal center. The first involves the HOMO of the CO molecule, Figure 28 left, which is the 5σ orbital that is primarly the lone pair on the carbon but is weakly antibonding with respect to the CO molecule. This becomes stabilized due to bonding interactions with the metal center and thus is involved in a σ-donor interaction which shifts electron density into unoccupied orbitals on the metal center. These bonding interactions involve the metal 3d and 4s orbitals[101] and are described by the secular determinant given in eq 8. Here E_{4s} and E_{3d} are the energies of the metal 4s and

$$\begin{vmatrix} E_{4s}-E & H_{4s,3d} & H_{4s,5\sigma} \\ H_{4s,3d} & E_{3d}-E & H_{3d,5\sigma} \\ H_{4s,5\sigma} & H_{3d,5\sigma} & E_{5\sigma}-E \end{vmatrix} = 0 \qquad (8)$$

3d orbitals, $E_{5\sigma}$ is the energy of the CO 5σ HOMO, and $H_{4s,5\sigma}$, etc., are the interaction matrix elements which in the Wolfberg–Helmholtz approximation are proportional to the overlap of the corresponding orbitals. For a d^{10} metal or metal ion (Ni(0), Cu(I), Zn(II)) the d band is fully occupied, so it can make no net contribution to bonding. Thus the dominant bonding interaction involves the CO 5σ with the unoccupied metal 4s orbital which is raised in energy due to this σ donor interaction (Figure 28 left, bottom).

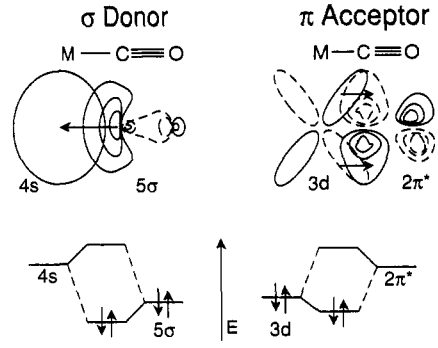

Figure 28. Molecular orbital description of CO bonding to a metal center. The 5σ (HOMO) orbital of the CO molecule (left) becomes stabilized due to its σ donor interaction with the metal 4s. The 2π* orbital (LUMO) of CO (right) is destabilized and accepts metal 3d electron density stabilizing the d band.

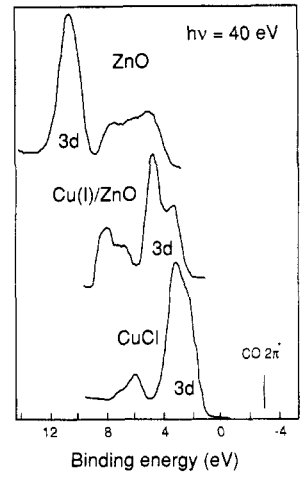

Figure 29. Comparison of d^{10} metal ion oxide and chloride valence band spectra. The valence band spectra of ZnO-(10$\bar{1}$0) (top), Cu(I)/ZnO(0001) (middle), and CuCl(111) (bottom) are taken at $h\nu$ = 40 eV, aligned to their respective Fermi levels. The approximate energy of the CO 2π* (2.6 and ~3 eV above the Fermi level for CO/CuCl and CO/ZnO, respectively) is indicated at bottom.

The second bonding interaction to a metal ion site involves the 2π*(LUMO) of CO which is at high energy relative to the d band of the substrate. Upon interaction, the d band becomes stabilized in energy and thus the CO acts as a π-acceptor ligand shifting 3d electron density into the antibonding LUMO of the CO molecule (π backbonding).[102] The π-bonding interaction energies are given by the secular determinant (eq 9) where the matrix elements are as defined above.

$$\begin{vmatrix} E_{3d}-E & H_{3d,2\pi^*} \\ H_{3d,2\pi^*} & E_{2\pi^*}-E \end{vmatrix} = 0 \qquad (9)$$

The energy stabilization of the 3d level (or destabilization of the CO 2π* level) is given by $\Delta E \approx -(H_{3d,2\pi^*})^2/(E_{2\pi^*} - E_{3d})$; therefore the π-acceptor interaction (and the σ-donor interaction described above) increases as the interacting orbitals become closer in energy and have greater overlap. The photoelectron spectra of clean ZnO (Figure 7), Cu(I)/ZnO(0001) (Figure 25A), and CuCl (Figure 25C) taken at 40 eV photon energy are collected in Figure 29. From variable-energy photoelectron spectral data the d band of ZnO is at

deep binding energy (10–12 eV) while the d band for Cu(I)/ZnO(0001) is below the oxide valence band (at 2–6 eV). This difference in d orbital energy is due to the higher effective nuclear charge for Zn(II) which also leads to greater orbital contraction and less overlap.[39] Thus as indicated earlier, the d band for ZnO is ineffective in π backbonding into the CO $2\pi^*$ orbital which would be at ~ -3 eV in Figure 29. Alternatively for Cu(I) the d band is at low binding energy, and there should be less orbital contraction and better overlap, which increases the possibility of π backbonding. In addition, σ-donor energy denominators and orbital overlap should be different which could lead to a change in the CO 5σ donor interaction with Cu(I) relative to Zn(II) sites. Finally, from the bottom of Figure 29, CuCl(111) has the same general valence band energy distribution as Cu(I)/ZnO(0001) with d band at low binding energy CuCl(111) also has C_{3v} coordinatively unsaturated tetrahedral surface sites, and its chloride ligation has similar σ- and π-donor interactions with Cu(I) as does oxide ligation.[26] One can thus study CO binding to CuCl(111) as a model system for CO binding to Cu(I)/ZnO to probe these bonding interactions experimentally on a pure, well-defined surface.[103] Angle-resolved photoelectron spectral studies [38] show that CO binds along the coordinatively unsaturated direction of the Cu(I) site for CuCl(111) (as with the Zn(II) site of ZnO in Figure 22), and the temperature and pressure dependence of the 4σ intensity of CO bound to CuCl(111) (vide infra) give a ΔH_0 value of 23 kcal/mol, an analogous high affinity CO binding as found for the Cu(I) site on ZnO.

B. Experimental Probes of π Backbonding: Shake-Up Satellites

Chemisorption of CO on CuCl(111) results in the photoelectron spectrum given in Figure 30 (solid) which is superimposed on the clean (dashed) spectrum of the CuCl substrate. In addition to the presence of the 4σ, 1π, and 5σ peaks of the bound CO molecule (the energy position of the 1π and 5σ having been estimated from angle resolved photoelectron data), some d band intensity is found to shift from the low binding energy region to produce a shoulder on the deeper binding energy side of the d band. From the LUMO energy diagram in Figure 28, bottom, this reflects the presence of π backbonding for CO binding to Cu(I) sites on CuCl(111). A direct method to observe and quantify this backbonding is XPS studies of the carbon 1s peak of bound CO at ~292 eV. From Figure 31 in addition to the main peak associated with photoionization of the C 1s electron, there is a shake-up satellite in the spectrum of CO bound to CuCl.[38] This corresponds to an electron on the Cu(I) undergoing a metal to ligand $2\pi^*$ charge-transfer transition upon C 1s core ionization to partially charge compensate the hole produced on the CO molecule.[104–110] The intensity of the satellite reflects the efficiency of this process and is directly dependent on the π-backbonding interaction between the metal d and CO $2\pi^*$ orbitals. The fact that CO bound to Cu(I) exhibits a satellite with significant intensity (50% that of the main peak) demonstrates the presence of π backbonding for this surface complex, and the lack of measurable satellite intensity for CO

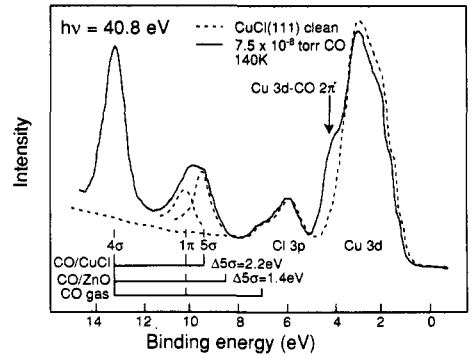

Figure 30. Chemisorption of CO on CuCl(111): 40.8 eV PES spectra of CuCl(111) clean (dashed) and in a 7.5×10^{-8} torr ambient of CO at 140K (solid). Position of the CO 4σ, 1π, and 5σ are indicated along with a comparison to gas phase CO and CO chemisorbed to ZnO (see Figure 8). 1π and 5σ orbitals have been resolved by variable energy and angle resolved studies in ref 38.

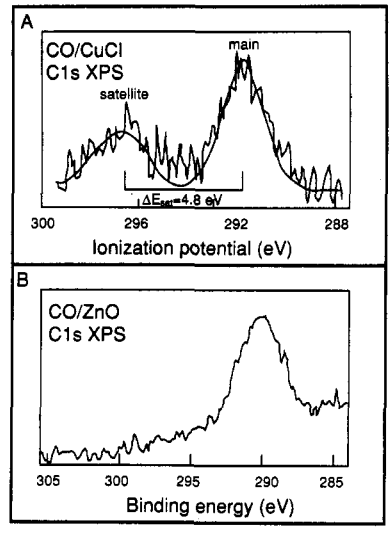

Figure 31. C1s XPS of CO on CuCl and ZnO: (A) CO/CuCl(111) at 140 K and 7.5×10^{-8} torr ambient CO; and (B) CO/ZnO($10\bar{1}0$) at 80 K and 5×10^{-6} torr ambient CO. Part A was taken with Mg Kα X-ray source, and part B was taken with 360-eV light from a synchrotron source.

bound to Zn(II) clearly confirms that there is no backbonding for CO chemisorbed to ZnO.[38]

On a more quantitative level, the π-backbonding matrix in eq 8 gives a bonding wave function $\psi^b = (\cos\theta)\psi_{3d} + (\sin\theta)\psi_{2\pi^*}$ where $\tan\theta = 2H_{3d,2\pi^*}/\Delta$ and $\Delta = E_{2\pi^*} - E_{3d}$. Upon ionization of a C 1s electron, final state relaxation occurs, shifting the CO $2\pi^*$ level to deeper energy by the amount U which corresponds to the electron–hole attraction (see Figure 32). The bonding interaction between the metal 3d and CO $\underline{2\pi^*}$ (which denotes the $2\pi^*$ level in the presence of a $\underline{\text{C}}$ 1s hole) leads to two different final states

$$\psi_s = (\cos\theta')\psi_{3d} - (\sin\theta')\psi_{2\pi^*}$$

and

$$\psi_m = (\sin\theta')\psi_{3d} + (\cos\theta')\psi_{2\pi^*}$$

with $\tan 2\theta' = 2H_{3d,2\pi^*}/(\Delta - U)$. These final states correspond to the main (ψ_m) and satellite (ψ_s) peaks in the C 1s XPS spectra in Figure 31 with a main peak to

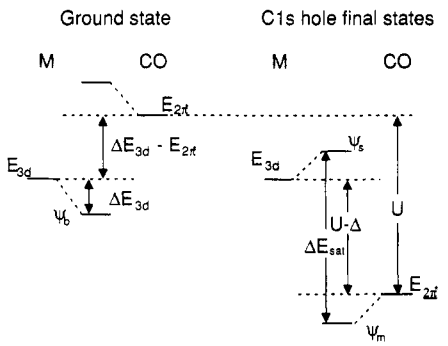

Figure 32. Effects of C 1s core ionization on the metal 3d–CO $2\pi^*$ energy level diagram: CO/CuCl ground state (left) and two C1s ionized final states (right). CO $2\pi^*$ is located above the Fermi level in the ground state but is relaxed to below the d levels by an energy U when a C1s hole is created by photoionization (indicated as $2\pi^*$). Two final states result from the interaction of the M 3d and CO $2\pi^*$. For the screened final state, charge is transferred from the Cu 3d into the CO $2\pi^*$ level. The photoelectrons produced from the screened final state have higher kinetic energy (thus, lower binding energy) and correspond to the main peak (Ψ_m). The photoelectrons from the unscreened state are at lower kinetic energy and correspond to the satellite peak (Ψ_s) at higher binding energy, ΔE_{sat}.

satellite peak energy separation, ΔE_{sat}, and intensity ratio, I_s/I_m,[106,111] give by eq 10, parts a and b.

$$\Delta E_{sat} = [(\Delta - U)^2 + 4(H_{3d,2\pi^*})^2]^{1/2} \qquad (10a)$$

$$I_s/I_m = [(\sin\theta' \cos\theta - \cos\theta' \sin\theta)/(\cos\theta' \cos\theta + \sin\theta' \sin\theta)]^2 = \tan^2(\theta' - \theta) \qquad (10b)$$

Finally, it is important to note that the C 1s XPS data in Figure 31 can be used to estimate the effective atomic charge on the carbon of the chemisorbed CO.[112,113] According to the sudden approximation, the binding energy of the C 1s peak in the initial state is the photoelectron intensity weighted average energy including both the main and satellite peaks.[114,115] For CO/CuCl(111) this is 293.4 eV. For CO/ZnO there is no satellite intensity, but referencing to the vacuum level yields an ionization energy of 294.5 eV. The C 1s ionization energy for gas-phase CO is 295.9 eV.[112] Thus CO bound to both surfaces has a C 1s binding energy below that of the gas-phase value which seems to indicate a shift of negative charge to the carbon upon chemisorption. However, the binding energy shifts observed for bonding to the surface include a relaxation shift to lower binding energy which must be subtracted to determine the chemical shift associated with chemisorption. X-ray-induced Auger and valence band photoelectron data give core relaxation shifts of −2.9 eV for CO/CuCl and −2.0 eV for CO/ZnO.[38] Therefore, corrected for relaxation, the C 1s binding energy for CO, in fact, increases upon chemisorption by +0.4 eV for CO/CuCl and +0.6 eV for CO/ZnO. These chemical shifts relative to gas-phase CO can be used in the charge potential model developed by Siegbahn and Jolly[112,113,116,117] to estimate the net increase in positive charge on the carbon of chemisorbed CO. These are found to be +0.10 for CO/CuCl and +0.14 for CO/ZnO and will be discussed in section VIII.

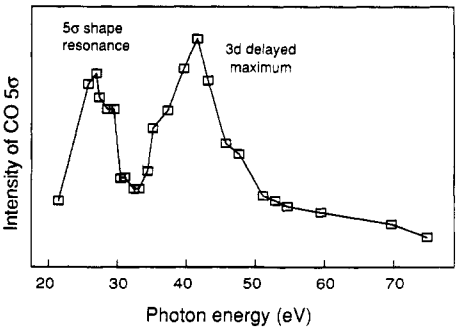

Figure 33. 5σ intensity vs photon energy for CO/CuCl(111), 9000 L CO, 80 K.

C. Experimental Probes of σ-Donor Bonding: Resonance Photoelectron Spectroscopy

As seen in Figure 28, left, the σ-donor interaction of CO with the metal center should stabilize its 5σ orbital to deeper binding energy. This stabilization is observed for CO binding to CuCl (Figure 30) where the 2.2 eV shift in the 5σ peak energy is significantly larger than the 1.4 eV shift estimated for CO bonding to ZnO (vide supra). However, for CuCl this stabilization is complicated by the fact that the 5σ orbital can interact with the metal 3d band which will stabilize the 5σ orbital energy but not contribute to bonding as both the 5σ and 3d levels are fully occupied. The variable-energy photoelectron data for the 5σ peak intensity in Figure 33 show that some interaction of the 5σ with the 3d band does, in fact, occur.[38] In addition to the shape resonance associated with the free CO molecule,[118,119] there is a delayed maximum in the 5σ cross section peaking at ~41 eV which is associated with metal d character covalently mixed into the 5σ CO molecular orbital. Alternatively, from Figure 28, left, the energy destabilization of the unoccupied metal 4s orbital should directly probe the σ donor interaction of the CO, and this can be studied by resonance photoelectron spectroscopy.

Figure 34 presents the valence photoelectron spectrum of clean CuCl extended to deeper binding energy. At 17-eV binding energy there is a satellite peak which has significant intensity only when the photon energy is scanned through the 75–80-eV region and thus is resonance enhanced.[120,121] As given by eq 11, parts a–c, this satellite peak corresponds to a Cu 3d → 4s shake-up transition on the 3d ionization.

main peak

$$\text{Cu(I) } 3p^6 3d^{10} \xrightarrow{h\nu} 3p^6 3d^9 \qquad (11a)$$

satellite

$$\text{Cu(I) } 3p^6 3d^{10} \xrightarrow{h\nu} 3p^6 3d^8 4s^1 \qquad (11b)$$

resonance

$$\text{Cu(I) } 3p^6 3d^{10} \xrightarrow{h\nu} 3p^5 3d^{10} 4s^1 \xrightarrow{\text{Auger}} 3p^6 3d^8 4s^1 \qquad (11c)$$

The satellite has little intensity at nonresonance photon energies since it corresponds to a two-electron transition and there is little change in 3d/4s mixing on 3d

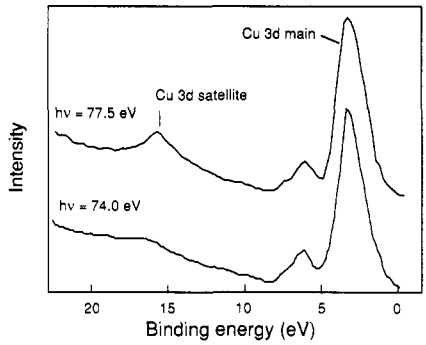

Figure 34. Resonance enhancement of the Cu shake-up satellite in the valence band PES spectrum of CuCl(111).

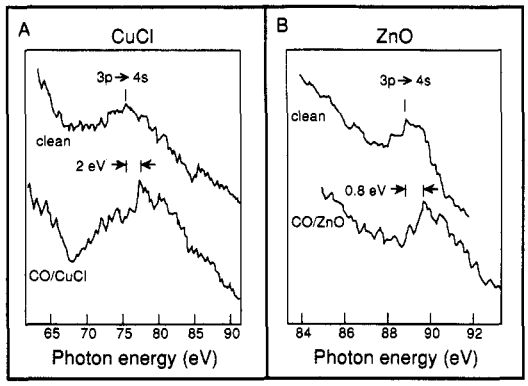

Figure 35. Shake-up satellite intensity as a function of photon energy for clean and CO covered (A) CuCl(111) and (B) ZnO(1010) surfaces. Intensity is resonance enhanced at the M 3p → 4s absorption edge. Note the energy scales are different for A and B.

ionization. However, the satellite becomes resonance enhanced at the copper M edge (3p → 4s) at ~77.5 eV. As given in eq 11c the resonance process involves photoexcitation of a 3p electron into the unoccupied 4s orbital. This excited state then undergoes an efficient super Coster–Kronig Auger[122] decay process involving two d electrons which have a large repulsive interaction resulting in the $3p^6\ 3d^8\ 4s^1$ final state associated with the shake-up satellite. Thus the resonance enhancement of the shake-up satellite profiles the Cu 3p → 4s transition with high surface sensitivity (~50 eV kinetic energy for the ejected electron).

Figure 35A plots the intensity of the shake-up satellite as a function of photon energy through the 3p → 4s absorption edge. For clean CuCl the absorption M edge is at 77 eV. CO chemisorption results in a 2 eV shift of the 3p → 4s transition to higher transition energy. Since the energy of the Cu 3p orbital is not changed upon chemisorption, this indicates that the Cu 4s orbital has been destabilized by 2 eV due to its σ bonding interaction with the CO 5σ level as indicated in Figure 28, left. The equivalent data for CO binding to ZnO is given in Figure 35B. For clean ZnO the 3p → 4s absorption edge is at 89 eV. CO chemisorption results in a 0.8 eV shift of the 4s orbital to higher energy. Therefore, in addition to the presence of π backbonding, CO binding to Cu(I) sites undergoes a stronger σ-donor interaction relative to CO binding to Zn(II) sites. These differences in bonding have significant consequences with respect to the physical properties of the chemisorbed CO molecule and are of relevance to catalysis as discussed in the next section.

Table IV. Comparison of Electronic and Physical Properties of CO Binding to Zn(II), Cu(I), and Ni(0) d^{10} Metal Ion Sites

physical property	ZnO(10$\bar{1}$0)	CuCl(111)	Ni(100)
ΔH_o (kcal/mol)	12	23	28
$\Delta\phi$ (eV)	−1.2	−0.8	+1.0
ΔL_{C-O} (Å)	−0.03	−0.02	+0.03
ΔQ (unit charge)	+0.14	+0.10	−0.05

VIII. Relevance to Catalysis

The stronger σ-donor interaction and the additional presence of π backbonding together increase the strength of the CO surface bond for Cu(I) relative to Zn(II) sites. This would increase the concentration of surface bound CO on Cu(I)-promoted catalysts and increase the reaction rate. From Table IV the heat of absorption of CO binding to Cu(I) sites is double that for Zn(II) binding and approaches the value for CO binding to Ni(0) surface sites. However, the CO–surface bond for Zn(II) and Cu(I) sites is fundamentally different from that for CO binding the metal surface sites in that it is dominated by the σ-donor interaction. From Table IV the strong CO–π backbonding on the Ni(0) surface leads to net charge transfer from the surface to the CO molecule; hence, the work function (Φ) increases, and the effective atomic charge on the carbon (ΔQ) becomes more negative relative to gas phase. The strong π backbonding weakens the CO bond leading to an increase in CO bond length (ΔL_{C-O}) from NEXAFS studies. Alternatively, for CO bonding to both Cu(I) and Zn(II) sites, charge is donated to the surface leading to a decrease in work function, a net positive charge on the carbon, and a shorter and stronger CO bond. Thus both Cu(I) and Zn(II) sites are particularly well suited for selectively reducing CO to methanol. The increased strength of the CO bond upon chemisorption is consistent with CO bond retention in product formation. In addition, chemisorption on both Zn(II) and Cu(I) sites leads to positive charge on the carbon which activates the CO for nucleophilic attack by hydride which is present on ZnO surfaces as a result of the heterolytic dissociation of dihydrogen.[123]

The relaxation corrected carbon 1s XPS data in section VII.b allow an estimate of the relative positive charge on the carbon for CO bound to Zn(II) and Cu(I) sites. From Table IV the carbon is more positive for CO binding to Zn(II) sites indicating that the role of Cu(I) in promoting methanol synthesis by lowering the activation barrier for catalysis is not simply electrostatic activation of the hydride attack in Scheme I (which is a modified version of the Costa and Muetterites mechanisms).[124-126] The role of Cu(I) would appear to relate to the stabilization of a subsequent transition state in the reaction. The rate-determining step in Scheme I is considered to be the generation of the formaldehyde complex 4 which is thermodynamically uphill.[125,127,128] The key difference in the bonding of CO to Cu(I) relative to Zn(II) sites is stronger σ donation and the additional presence of some π backbonding. For a d^{10} ion neither is expected to play a significant role in the formation of formyl (species 3) via species 2.[38,129] Alternatively, the presence of d–π backbonding into unoccupied π^* orbitals of the ligand will significantly stabilize this formyl level intermediate 3 and the η^2-bidentate formaldehyde species 4 bound to the

Scheme I

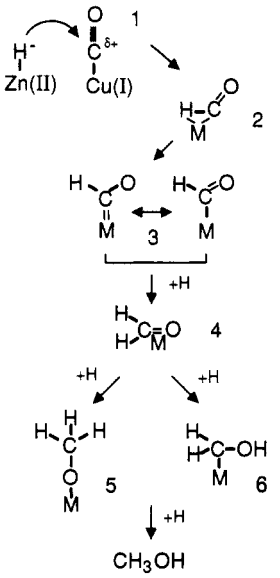

Cu(I) active site. In particular, d–π backbonding should increase the carbene character present in intermediate **3** which would assist in proton attack to produce formaldehyde. While species **5** and **6** do not appear to be involved in the rate-determining step in methanol synthesis, Baetzold[130] has calculated that the methoxy species **5** is also stabilized by bonding to Cu(I). Thus in contrast to the behavior on metals, σ donation dominates the CO/Cu(I) bond while the presence of some π backbonding can stabilize key intermediates involved in formaldehyde formation. Cu(I) appears to be electronically well suited for CO activation in methanol synthesis.

Before concluding this section, it should be pointed out that studies[131] have been reported which suggest that methanol is synthesized from CO_2 ($CO_2 + 3H_2 \rightarrow CH_3OH + H_2O$) on $Cu/ZnO/Al_2O_3$ catalysts under industrial conditions. This reaction is thought to occur via the following steps:

$$CO_2^-{}_{(a)} + H_{(a)} \rightarrow HCO_2^-{}_{(a)} \quad (12a)$$

$$HCO_2^-{}_{(a)} + 2H_{(a)} \rightarrow CH_3O^-{}_{(a)} + O_{(a)} \quad (12b)$$

$$CH_3O^-{}_{(a)} + H_{(a)} \rightarrow CH_3OH_{(g)} \quad (12c)$$

where breaking the carbon–oxygen bond in the formate species is likely the rate-determining step.[79,132] The relevance of this reaction to CO hydrogenation chemistry is complicated by the fact that the Cu/ZnO system is also a water–gas shift catalyst:[133]

$$CO + H_2O \rightarrow CO_2 + H_2 \quad (13)$$

The ICI group have used radiolabeled CO or CO_2 under reaction conditions where methanol synthesis proceeded faster than the reverse water–gas shift reaction and found the carbon in the methanol to be derived from CO_2.[131] In contrast Ren et al.[134] utilizing a similar experimental arrangement, found that CO_2 formed methanol more slowly than CO. Further, through the use of chemical trapping and isotopically labeled CO and H_2O, Klier et al.[135] have reported that under their experimental conditions CO and not CO_2 is the primary source of carbon for methanol. Thus the roles of CO and CO_2 over $Cu/ZnO/Al_2O_3$ catalysts in the methanol synthesis reaction remain somewhat controversial. The studies described in this review only address the interaction of CO with Cu(I) and Zn(II) sites. Further surface studies are required to define the nature of the species involved in the water–gas shift chemistry and their relevance to the intermediates involved in CO methanol catalysis.

IX. Summary and Future Directions

Cu(I) and Zn(II) d^{10} metal ion surface sites appear to be particularly well suited for methanol synthesis from CO in that both have a dominant σ-donor interaction which strengthens the CO bond and activates the carbon for nucleophilic attack by hydride. Cu(I) has the additional advantage of some π backbonding which can stabilize intermediates related to the activation barrier for catalysis. A number of important problems remain including understanding the electronic structures of the species in Scheme I bound to d^{10} metal ions and, in general, spectroscopically defining the surface intermediates involved in methanol synthesis and water–gas shift chemistry on cuprous oxide and zinc oxide surfaces. In addition, there is the interesting question as to the relative effectiveness of the chemically different surface structures in Figure 2 in the heterolytic cleavage of dihydrogen. Finally, on a more general level, the above studies have focused on the binding of organometallic ligands to coordination compound metal oxide surfaces. No change in surface metal ion oxidation state has been implicated in this chemistry. From Table I metal oxides are extensively utilized as oxidation catalysts. It will be extremely interesting to define the surface oxygen and organic substrate intermediates involved in this nucleophilic oxidation chemistry and the redox processes associated with the surface metal ion in contrast to metals (such as Ag) which catalyze the electrophilic oxidation of substrates, and to understand how these relate to parallel homogeneous and biological oxidation catalysis.

X. Abbreviations

PES	photoelectron spectroscopy
IR	infrared spectroscopy
LEED	low-energy electron diffraction
SCF-Xα-SW	self-consistent field Xα-scattered wave
ERPS	extramolecular relaxation polarization shift
CMA	cylindrical mirror analyzer
EDC	energy distribution curve
HREELS	high-resolution electron energy-loss spectroscopy
NEXAFS	near-edge X-ray absorption fine structure
XPS	X-ray photoelectron spectroscopy
ML	monolayer
EXAFS	extended X-ray absorbtion fine structure
XAS	X-ray absorption spectroscopy

HOMO	highest occupied molecular orbital
LUMO	lowest unoccupied molecular orbital
eV	electron volt

XI. Acknowledgments

This research is supported by the NSF MRL program at the Center for Materials Research at Stanford University. Support for the work done at the Stanford Synchrotron Radiation Laboratory, which is operated by the Department of Energy Division of Chemical Sciences, is gratefully acknowledged. E.I.S. would like to thank his students (Bob Gay, Kevin D'Amico, Susan Cohen, Lung-Shan Kau, Steve Didziulis, Kris Butcher, and Jianyi Lin) and his collaborators (Vic Henrich, Herb Zeiger, and Reed McFeely) for their contributions to various phases of this research. P.M.J. would like to acknowledge the IBM Corporation for its financial support.

XII. References

(1) Solomon, E. J.; Gerwirth, A. A.; Cohen, S. L. In *Understanding Molecular Properties*; Hansen, A. E., Avery, J., Dahl, J. P., Eds.; Dordrecht: Reidel, 1987; pp 27–68.
(2) *Photoemission in Solids II*; Cardona, M., Ley, L., Eds.; Springer-Verlag: Berlin, 1979.
(3) *Photoemission in Solids I*; Cardona, M., Ley, L., Eds.; Springer-Verlag: Berlin, 1978.
(4) Ghosh, P. *Introduction to Photoelectron Spectroscopy*; John Wiley and Sons: New York, 1983.
(5) Seah, M. P. *Practical Surface Analysis*, 2nd ed.; Wiley: Chichester, 1990.
(6) Lindau, I.; Spicer, W. E. *J. Electron Spectrosc. Related Phenom.* **1974**, *3*, 409–413.
(7) Gay, R. R.; Nodine, M. H.; Henrich, V. E.; Zeiger, H. J.; Solomon, E. I. *J. Am. Chem. Soc.* **1980**, *102*, 6752–6761.
(8) Allyn, C. L.; Gustafsson, T.; Plummer, E. W. *Solid State Commun.* **1978**, *28*, 85–89.
(9) Andersson, S. *Solid State Commun.* **1977**, *21*, 75–81.
(10) Horn, K.; Bradshaw, A. M.; Jacobi, K. *Surf. Sci.* **1978**, *72*, 719–732.
(11) Hush, N. S.; Williams, M. L. *J. Mol. Spectrosc.* **1974**, *50*, 349–368.
(12) Boccuzzi, F.; Garrone, E.; Zecchina, A.; Bossi, A.; Camia, M. *J. Catal.* **1978**, *51*, 160–168.
(13) Waddams, A. L. *Chemicals from Petroleum: An Introductory Survey*, 3rd ed.; John Wiley and Sons: New York, 1973.
(14) Lüth, H.; Rubloff, G. W.; Grobman, W. D. *Solid State Commun.* **1976**, *18*, 1427–1430.
(15) Nyholm, R. S. *Proc. Chem. Soc., London* **1961**, 273–296.
(16) Burzyk, J.; Haber, J. *Bull. Acad. Pol. Sci. Ser. Sci. Chim.* **1969**, *17*, 531–538.
(17) Burzyk, J.; Haber, J.; Nowotny, J. *Bull. Acad. Pol. Sci. Ser. Sci. Chim.* **1969**, *17*, 543–550.
(18) Klier, K. *Adv. Catal.* **1982**, *31*, 243–313.
(19) Natta, G. *Catalysis* **1955**, *3*, 349–411.
(20) Abrahams, S. C.; Bernstein, J. L. *Acta Crystallogr., Sect. B* **1969**, *B25*, 1233–1236.
(21) Duke, C. B.; Meyer, R. J.; Paton, A.; Mark, P. *Phys. Rev. B.* **1978**, *18*, 4225–4240.
(22) Lubinsky, A. R.; Duke, C. B.; Chang, S. C.; Lee, B. W.; Mark, P. *J. Vac. Sci. Technol.* **1976**, *13*, 189–192.
(23) Henzler, M. *Surf. Sci.* **1973**, *36*, 109–122.
(24) Henrich, V. E.; Zeiger, H. J.; Solomon, E. I.; Gay, R. R. *Surf. Sci.* **1978**, *74*, 682–683.
(25) Tossell, J. A. *Inorg. Chem.* **1977**, *16*, 2944–2949.
(26) Didziulis, S. V.; Cohen, S. L.; Butcher, K. D.; Solomon, E. I. *Inorg. Chem.* **1988**, *27*, 2238–2250.
(27) Manson, S. T. In *Photoemission in Solids I*; Cardona, M., Ley, L., Eds.; Springer-Verlag: Berlin, 1978; pp 135–163.
(28) Solomon, E. I. *Comments Inorg. Chem.* **1984**, *3*, 227–320.
(29) Yeh, J. J.; Lindau, I. *At. Data Nucl. Data Tables* **1985**, *32*, 1–155.
(30) Fano, U.; Copper, J. W. *Rev. Mod. Phys.* **1968**, *40*, 441–507.
(31) Eastman, D. E.; Kuznietz, M. *J. Appl. Phys.* **1971**, *42*, 1396–1402.
(32) Manson, T. M.; Copper, J. W. *Phys. Rev.* **1968**, *165*, 126–138.
(33) Copper, J. W. *Phys. Rev.* **1962**, *128*, 618–693.
(34) Rubloff, G. W.; Grobman, W. D.; Lüth, H. *Phys. Rev. B* **1976**, *14*, 1450–1457.
(35) Shirley, D. A. *J. Vac. Sci. Technol.* **1975**, *12*, 280–285.
(36) Gay, R. R. Ph.D. Thesis, M.I.T., 1979.
(37) Ivanov, I.; Pollman, J. *Phys. Rev. B* **1981**, *24*, 7275–7296.
(38) Lin, J.; Jones, P.; Guckert, J.; Solomon, E. I. *J. Am. Chem. Soc.* **1991**, *113*, 8312–8326.
(39) Lin, J.; Jones, P. M.; Lowery, M. D.; Gay, R. R.; Cohen, S. L.; Solomon, E. I. *Inorg. Chem.* **1992**, *31*, 686–695.
(40) Morimoto, T.; Yanai, H.; Nagao, M. *J. Phys. Chem.* **1976**, *80*, 471–475.
(41) Tsyganenko, A. A.; Pozdnyakov, D. V.; Filimonov, V. N. *J. Mol. Struct.* **1975**, *29*, 299–318.
(42) Turner, D. W.; Baker, C.; Baker, A. D.; Brundle, C. R. *Molecular Photoelectron Spectroscopy*; Wiley-Intersciences: London, 1970, pp 364.
(43) Davenport, J. W. Ph.D. Thesis, University of Pennsylvania, 1976.
(44) Hayward, D. O.; Trapnell, B. M. W. *Chemisorption*, 2nd ed.; Butterworths: Washington, 1964.
(45) Smith, N. V. In *Photoemission in Solids I*; Cardona, L., Ley, L., Eds.; Springer-Verlag: Berlin, 1978; pp 237–264.
(46) Sayers, M. J.; McCellen, M. R.; Gay, R. R.; Solomon, E. I.; McFeely, F. R. *Chem. Phys. Lett.* **1980**, *75*, 575–578.
(47) D'Amico, K. L.; Trenary, M.; Shinn, N. D.; Solomon, E. I.; McFeely, F. R. *J. Am. Chem. Soc.* **1982**, *104*, 5102–5105.
(48) McCellan, M. R.; Trenary, M.; Shinn, N. D.; Sayers, M. J.; D'Amico, K. L.; Solomon, E. I.; McFeely, F. R. *J. Chem. Phys.* **1981**, *74*, 4726–4731.
(49) Note: It should be noted that this result does not support a recent study[50] on a similarly prepared ZnO(000$\bar{1}$)–oxide surface which assumes a CO bonding geometry normal to the surface plane.
(50) Au, C. T.; Hirsch, W.; Hirschwald, W. *Surf. Sci.* **1988**, *197*, 391–401.
(51) Thomas, J. M.; Thomas, W. J. *Introduction to the Principles of Heterogeneous Catalysis*; Academic Press: London, 1967.
(52) Ibach, H.; Mills, D. L. *Electron Energy Loss Spectroscopy and Surface Vibrations*; Academic Press: New York, 1982.
(53) Ibach, H. *Phys. Rev. Lett.* **1970**, *24*, 1416–1418.
(54) Ibach, I. *J. Vac. Sci. Technol.* **1972**, *9*, 713–719.
(55) Many, A.; Gersten, J. I.; Wagner, I.; Rosenthal, A.; Goldstein, Y. *Surf. Sci.* **1982**, *113*, 355–361.
(56) D'Amico, K. L.; McFeely, F. R.; Solomon, E. I. *J. Am. Chem. Soc.* **1983**, *105*, 6380–6383.
(57) Herzberg, G. *Molecular Spectra and Molecular Structure II: Infrared and Raman Spectra of Polyatomic Molecules*; Van Nostrand Reinhold Company: New York, 1945.
(58) Dixon, R. N. *Spectroscopy and Structure*; John Wiley and Sons: New York, 1965.
(59) Hopster, H.; Ibach, H. *Surf. Sci.* **1978**, *77*, 109–117.
(60) Sexton, B. A. *Chem. Phys. Lett.* **1979**, *63*, 451–454.
(61) Dehmer, J. L.; Dill, D. *J. Chem. Phys.* **1976**, *65*, 5327–5334.
(62) Stöhr, J.; Jaeger, R. *Phys. Rev. B* **1982**, *26*, 4111–4131.
(63) Stöhr, J.; Gland, J. L.; Eberhardt, W.; Outka, D.; Madix, R. J.; Sette, F.; Koestner, R. J.; Doebler, U. *Phys. Rev. Lett.* **1983**, *51*, 2414–2417.
(64) Stöhr, J. In *The Structure of Surfaces*; Van Hove, M. A., Tong, S. Y., Eds.; Springer-Verlag: Berlin, 1985.
(65) Stöhr, J. *NEXAFS Spectroscopy*; Springer-Verlag: New York, 1992.
(66) Stöhr, J.; Kollin, E. B.; Dwyer, J. L.; Gland, J. L.; Robins, J. L.; Johnson, A. L. *Phys. Rev. Lett.* **1985**, *54*, 935–938.
(67) Dominquez, J. M.; Simmons, G. W.; Klier, K. *J. Mol. Catal.* **1983**, *20*, 369–385.
(68) Bulko, J. B.; Herman, R. G.; Klier, K. *J. Phys. Chem.* **1979**, *83*, 3118–3122.
(69) Goodby, J. E.; Pemberton, J. E. *Appl. Spectrosc.* **1988**, *42*, 754–760.
(70) Ruggeri, O.; Trifiro, F.; Vaccari, A. *Solid State Commun.* **1982**, *42*, 120–124.
(71) Moretti, G.; De Rossi, S.; Ferraris, G. *Appl. Surf. Sci.* **1990**, *45*, 341–349.
(72) Okamoto, Y.; Fukino, K.; Imanaka, T.; Teranishi, S. *J. Phys. Chem.* **1983**, *87*, 3740–3746.
(73) Kau, L.; Hodgson, K. O.; Solomon, E. I. *J. Am. Chem. Soc.* **1989**, *111*, 7103–7109.
(74) Peplinski, B.; Unger, W. E. S.; Grohmann, I. *Appl. Surf. Sci.* **1992**, *62*, 115–129.
(75) Okamoto, Y.; Fukino, K.; Imanaka, T.; Teranishi, S. *J. Phys. Chem.* **1983**, *87*, 3747–3754.
(76) Denise, B.; Sneeden, R. P. A.; Beguin, B.; Cherifi, O. *Appl. Catal.* **1987**, *30*, 353–363.
(77) Chinchen, G. C.; Waugh, K. C.; Whan, D. A. *Appl. Catal.* **1986**, *25*, 101–107.
(78) Chinchen, G. C.; Waugh, K. C. *J. Catal.* **1986**, *97*, 280–283.
(79) Chinchen, G. C.; Mansfield, K.; Spencer, M. S. *CHEMTECH* **1990**, *20*, 692–699.
(80) Klier, K. *Adv. Catal.* **1982**, *31*, 243–313.
(81) Rodriguez, J. A.; Campbell, C. T. *J. Phys. Chem.* **1987**, *91*, 6648–6658.
(82) Didziulis, S. V.; Butcher, K. D.; Cohen, S. L.; Solomon, E. I. *J. Am. Chem. Soc.* **1989**, *111*, 7110–7123.
(83) Wertheim, G. K.; DiCenzo, S. B.; Youngquist, S. E. *Phys. Rev. Lett.* **1983**, *51*, 2310–2313.
(84) Scrocco, M. *Chem. Phys. Lett.* **1979**, *63*, 52–56.

(85) Robert, T. *Chem. Phys.* **1975**, *8*, 123–135.
(86) Cox, D. F.; Schulz, K. H. *Surf. Sci.* **1991**, *249*, 138–148.
(87) Note: There is some controversy concerning Cu overlayers on the (000$\bar{1}$)-oxide surface. Campbell et al.[88] believe that submonolayer coverages form islands with the CO binding in a manner similar to that observed on Cu metal. However, in our experiments submonolayer copper coverages deposited by evaporation onto a room temperature ZnO(000$\bar{1}$)-oxide substrate appear dispersed and no 4σ intensity is observed upon CO exposure to a 0.3 ML Cu/ZnO(000$\bar{1}$)–oxide surface. Under our conditions a 4σ peak intensity of three times less than that observed for CO on 0.3 ML Cu/ZnO-(0001)-zinc in spectrum a of Figure 24B would have been measurable. However, at higher copper coverages on this surface we do observe 4σ intensity and a UPS spectrum indicative of CO chemisorption to metallic copper.
(88) Ernst, K. H.; Ludviksson, A.; Zhang, R.; Campbell, C. T. *J. Catal.* **1993**, in press.
(89) Ghijsen, J.; Tjeng, L. H.; van Elp, J.; Eskes, H.; Westerink, J.; Sawatzky, G. A. *Phys. Rev. B* **1988**, *38*, 11322–11330.
(90) Pong, W.; Okada, S. K. *Phys. Rev. B* **1979**, *20*, 5400–5403.
(91) Sorrell, T. N.; Jameson, D. L. *J. Am. Chem. Soc.* **1983**, *105*, 6013–6018.
(92) Sorrell, T. N.; Malachowski, M. R. *Inorg. Chem.* **1983**, *22*, 1883–1887.
(93) Note: Previous EXAFS and XAS studies have yielded conflicting results regarding the distribution of copper in the active catalyst. Several studies[94,95] have reported the presence of only Cu(0) in the reduced binary catalyst, with extensive copper clustering predominating at high temperatures.[94] In another study, in situ EXAFS spectroscopy was performed on a 30% Cu-reduced catalyst[96] below 400 K two forms of copper coexisted (Cu(0) and Cu(I)) with a Cu–O bond present in the interfacial region, while above 400 K only small copper metal clusters were observed. However, a recent XPS study[71] on a 5% Cu catalyst reduced at 473 K reports the presence of a Cu(I) species stabilized by the support. Another EXAFS study[97] using 10–33% Cu catalysts reduced at 523 K reports the presence of three phases: Cu metal, a Cu_2O-like phase, and interstitial Cu(I) with both the Cu_2O-like phase and the interstitial phase having the same bond length.
(94) Clausen, B. S.; Lengeler, B.; Rasmussen, B. S.; Niemann, W.; Topsøe, H. *J. Phys. (Paris)* **1986**, *C8*, 237–242.
(95) Vlaic, G.; Bart, J. C. J.; Cavigiolo, W.; Mobilio, S. *Chem. Phys. Lett.* **1980**, *76*, 453–459.
(96) Tohji, K.; Udagawa, Y.; Mizushima, T.; Ueno, A. *J. Phys. Chem.* **1985**, *89*, 5671–5676.
(97) Sankar, G.; Vasudevan, S.; Rao, C. N. R. *J. Chem. Phys.* **1986**, *85*, 2291–2299.
(98) Mantano, P. A.; Shenoy, G. K.; Alp, E. E.; Schulz, W.; Urban, J. *Phys. Rev. Lett.* **1986**, *56*, 2076–2079.
(99) Kau, L.; Penner-Hahn, J. E.; Solomon, E. I.; Hodgson, K. O. *J. Phys. (Paris)* **1986**, *47*, C8-1177–C8-1180.
(100) Kau, L.; Spira-Solomon, D. J.; Penner-Hahn, J. E.; Hodgson, K. O.; Solomon, E. I. *J. Am. Chem. Soc.* **1987**, *109*, 6433–6442.
(101) Note: The metal 4p level of σ symmetry will hybridize with the 4s level and contribute to this bonding interaction.
(102) Blyholder, G. *J. Phys. Chem.* **1964**, *68*, 2772–2778.
(103) Note: It should be noted that all spectral data obtained for CO binding to Cu(I)/ZnO are qualitatively similar to those reported below for CO/CuCl.
(104) Bagus, P. S.; Seel, M. *Phys. Rev. B* **1981**, *23*, 2065–2075.
(105) Brundle, C. R.; Bagus, P. S.; Menzel, D.; Hermann, K. *Phys. Rev. B* **1981**, *24*, 7041–7056.
(106) Gewirth, A. A.; Cohen, S. L.; Schugar, H. J.; Solomon, E. I. *Inorg. Chem.* **1987**, *26*, 1133–1146.
(107) Freund, H. J.; Plummer, E. W.; Salaneck, W. R.; Bigelow, R. W. *J. Chem. Phys.* **1981**, *75*, 4275–4281.
(108) Norton, P. J.; Tapping, R. L.; Goodale, J. W. *Surf. Sci.* **1978**, *72*, 33–44.
(109) Plummer, E. W.; Chen, C. T.; Ford, W. K.; Eberhardt, W.; Messmer, R. P.; Freund, H.-J. *Surf. Sci.* **1985**, *158*, 58–83.
(110) Umbach, E. *Surf. Sci.* **1982**, *117*, 482–502.
(111) van der Laan, G.; Westra, C.; Haas, C.; Sawatzky, G. A. *Phy. Rev. B* **1981**, *23*, 4369–4380.
(112) Siegbahn, K.; Nordling, C.; Johansson, G.; Hedman, J.; Hedén, P. F.; Hamrin, K.; Gelius, U.; Bergmark, T.; Werme, L. O.; Manne, R.; Baer, Y. *ESCA applied to Free Molecules*; North-Holland Publishing Company: Amsterdam, 1969.
(113) Jolly, W. L. *Faraday Discuss. Chem. Soc.* **1972**, *54*, 13–20.
(114) Didziulis, S. V.; Cohen, S. L.; Gerwirth, A. A.; Solomon, E. I. *J. Am. Chem. Soc.* **1988**, *110*, 250–268.
(115) Manne, R.; Åberg, T. *Chem. Phys. Lett.* **1970**, *7*, 282–284.
(116) Jolly, W. L.; Perry, W. B. *J. Am. Chem. Soc.* **1973**, *95*, 5442–5450.
(117) Jolly, W. L.; Perry, W. B. *Inorg. Chem.* **1974**, *13*, 2686–2692.
(118) Plummer, E. W.; Salaneck, W. R.; Miller, J. S. *Phys. Rev. B* **1978**, *18*, 1673–1701.
(119) Plummer, E. W.; Gustafsson, T.; Gudat, W.; Eastman, D. E. *Phys. Rev. B* **1977**, *15*, 2339–2355.
(120) Davis, L. C. *Phys. Rev. B* **1982**, *25*, 2912–2915.
(121) Ishii, T.; Taniguchi, M.; Kakizaki, A.; Naito, N.; Sugawara, H.; Hagakura, I. *Phys. Rev. B* **1986**, *33*,
(122) Davis, L. C.; Feldkamp, L. A. *Phys. Rev. B* **1981**, *23*, 6239–6253.
(123) Kokes, R. J. *Acc. Chem. Res.* **1973**, *6*, 226–233.
(124) Muetterties, E. L.; Stein, J. *Chem. Rev.* **1979**, *79*, 479–490.
(125) Fahey, D. R. *J. Am. Chem. Soc.* **1981**, *103*, 136–141.
(126) Costa, L. C. *Catal. Rev.-Sci. Eng.* **1983**, *25*, 325–363.
(127) Parker, D. G.; Pearce, R.; Prest, D. W. *J. Chem. Soc., Chem. Commun.* **1982**, 1193–1195.
(128) Collman, J. P.; Hegedus, L. S.; Norton, J. R.; Finke, R. G. *Principles and Applications of Organotransition Metal Chemistry*; University Science Books: Mill Valley, CA, 1987.
(129) Berke, H.; Hoffmann, R. *J. Am. Chem. Soc.* **1978**, *100*, 7224–7236.
(130) Baetzold, R. C. *J. Phys. Chem.* **1985**, *89*, 4150–4155.
(131) Chinchen, G. C.; Denny, P. J.; Parker, D. G.; Spencer, M. S.; Whan, D. A. *Appl. Catal.* **1987**, *30*, 333–338.
(132) Chinchen, G. C.; Spencer, M. S. *Catal. Today* **1991**, *10*, 293–301.
(133) Satterfield, C. N. *Heterogeneous Catalysis in Practice*; McGraw-Hill: New York, 1980.
(134) Ren, Z.; Wang, J.; Lu, D. *Appl. Catal.* **1989**, *49*, 83–90.
(135) Vedage, G. A.; Pritchai, R.; Herman, R. G.; Klier, K. In *Proceedings 8th International Congress on Catalysis*: Verlag Chemie: Berlin, 1984; Vol. 2; pp 47–58.
(136) Kung, H. H. *Transition Metal Oxides: Surface Chemistry and Catalysis*; Elsevier: Amsterdam, 1989; Vol. 45.
(137) Edwards, J. F.; Schrader, G. L. *J. Phys. Chem.* **1984**, *88*, 5620–5624.
(138) Edwards, J. F.; Schrader, G. L. *J. Catal.* **1985**, *94*, 175–186.
(139) Rozovskii, A. Y. *Kinet. Catal.* **1980**, *21*, 78–87.
(140) Saussey, J.; LaValley, J. C.; Lamotte, J.; Rais, T. *J. Chem. Soc., Chem. Commun.* **1982**, 278–279.
(141) Baidikova, I. V.; Khalil, A. E.; Vislovskii, V. P.; Mamedov, E. A. *Catal. Today* **1992**, *13*, 511–516.
(142) Bhattacharya, A. K.; Chand, S.; Mallick, K. K.; Talayan, R. S. *App. Catal. A: General* **1992**, *85*, 135–145.
(143) Choudhary, V. R.; Hare, V. H. *J. Catal.* **1991**, *130*, 411–422.
(144) Yang, X. C.; Bi, Y. L.; Zhen, K. J.; Wu, Y. *Catal. Today* **1992**, *13*, 543–548.
(145) McNamara, D. J.; Korf, S. J.; Seshan, K.; Van Ommen, J. G.; Ross, J. R. H. *Can. J. Chem. Eng.* **1991**, *69*, 883–890.
(146) Yamashita, H.; Machida, Y.; Tomita, A. *App. Catal. A: General* **1991**, *79*, 203–214.
(147) King, S. T. *J. Catal.* **1991**, *131*, 215–225.
(148) Zhou, B.; Chuang, K. T.; Guo, X. *J. Chem. Soc., Faraday Trans.* **1991**, *87*, 3696–3702.
(149) Burrington, J. D.; Kartisek, C. T.; Grasselli, R. K. *J. Catal.* **1984**, *87*, 363–380.
(150) Sachtler, W. M. *Catal. Rev.* **1970**, *4*, 27–50.
(151) Barr, T. L. *J. Vac. Sci. Technol. A* **1991**, *9*, 1793–1805.
(152) Ueda, W.; Oka, Y. M.; Ikawa, T. *J. Chem. Soc., Faraday Trans. 1* **1982**, *78*, 495–500.
(153) Trifiro, F.; Caputo, C.; Forzatti, P.; Pasquon, I. *J. Catal.* **1973**, *30*, 393–402.
(154) Rivasseau, J.; Cannesson, P.; Blanchard, M. *J. Phys. Chem.* **1980**, *84*, 2791–2795.
(155) Jonson, B.; Rebenstorf, B.; Larsson, R.; Andersson, S. L. T. *J. Chem. Soc., Faraday Trans. 1* **1988**, *84*, 3547–3566.
(156) Zhang, Z.; Henrich, V. E. *Surf. Sci.* **1992**, *277*, 263–272.
(157) Yao, Y. F. Y. *J. Catal.* **1973**, *28*, 139–149.
(158) Zagorenko, A. I.; Ivanova, O. P. *Surf. Interface Anal.* **1992**, *18*, 496–498.
(159) Jaenicke, S.; Chuah, G. K. *Ber. Bunsen-Ges. Phys. Chem.* **1992**, *96*, 1–9.
(160) Inomata, M.; Miyamaoto, A.; Murakami, Y. *J. Catal.* **1980**, *62*, 140–148.
(161) Voorhoeve, R. J. H.; Remeika, J. P.; Trimble, L. E.; Cooper, A. S.; Gallagher, P. K. *J. Sol. State Chem.* **1975**, *14*, 395–406.
(162) Loika, V. E.; Davydov, A. A. *J. Appl. Spectrosc.* **1988**, *49*, 709–712.
(163) Skupinska, J. *Chem. Rev.* **1991**, *91*, 613–648.
(164) Cockran, S. J.; Larkins, F. P. *J. Chem. Soc., Faraday Trans. 1* **1985**, *81*, 2179–2190.
(165) Taralas, G.; Vassilatos, V.; Sjostrom, K.; Delgado, J. *Can. J. Chem. Eng.* **1991**, *69*, 1413–1419.
(166) Petrie, W. T.; Vohs, J. M. *Surf. Sci. Lett.* **1991**, *259*, L750–L756.
(167) Wu, M. C.; Estrada, C. A.; Corneille, J. S.; Goodman, D. W. *J. Chem. Phys.* **1992**, *96*, 3892–3900.
(168) Smith, K. E.; Henrich, V. E. *Surf. Sci.* **1989**, *217*, 445–458.
(169) Henrich, V. E. Dresselhaus, G.; Zeiger, H. J. *J. Vac. Sci. Technol.* **1978**, *15*, 534–537.
(170) Henrich, V. E. Dresselhaus, G.; Zeiger, H. J. *Solid State. Commun.* **1977**, *24*, 623–626.
(171) Henrich, V. E.; Kurtz, R. L. *Phys. Rev. B* **1981**, *23*, 6280–6287.
(172) Smith, K. E.; Henrich, V. E. *Phys. Rev. B* **1985**, *32*, 5384–5390.
(173) Kurtz, R. L.; Henrich, V. E. *Phys. Rev. B* **1982**, *25*, 3563–3571.
(174) Kurtz, R. L.; Henrich, V. E. *Phys. Rev. B* **1982**, *26*, 6682–6689.
(175) Kurtz, R. L.; Henrich, V. E. *Phys. Rev. B* **1983**, *28*, 6699–6706.
(176) Smith, K. E.; Henrich, V. E. *Surf. Sci.* **1990**, *225*, 47–57.
(177) Kuhlenbeck, H.; Xu, C.; Dillmann, B.; Haßel, M.; Adam, B.; Ehrlich, D.; Wohlrab, S.; Freund, H. J.; Ditzinger, U. A.; Neddermeyer, H.; Neuber, M.; Neumann, M. *Ber. Bunsen-Ges. Phys. Chem.* **1992**, *96*, 15–27.

(178) Lad, R. J.; Henrich, V. E. *J. Vac. Sci. Technol. A* **1988**, *6*, 781–782.
(179) Kurtz, R. L.; Henrich, V. E. *Phys. Rev. B* **1987**, *36*, 3413–3421.
(180) Jeng, S. P.; Zhang, Z.; Henrich, V. E. *Phys. Rev. B* **1991**, *44*, 3266–3271.
(181) Mackay, J. L.; Henrich, V. E. *Phys. Rev. B* **1989**, *39*, 6156–6168.
(182) McKay, J. M.; Henrich, V. E. *Phys. Rev. B* **1985**, *32*, 6764–6772.
(183) Kuhlenbeck, H.; Odorfer, G.; Jaeger, R.; Illing, G.; Menges, M.; Mull, T.; Freund, H. J.; Pohlchen, M.; Staemmler, V.; Witzel, S.; Scharfschwerdt, C.; Wennemann, K.; Liedtke, T. *Phys. Rev. B.* **1991**, *43*, 1969–1986.
(184) Petrie, W. T.; Vohs, J. M. *Surf. Sci.* **1991**, *245*, 315–323.
(185) Ferrer, S.; Somorjai, G. A. *Surf. Sci.* **1980**, *94*, 41–56.